Date of publication xxxx 00, 0000, date of current version xxxx 00, 0000.
Digital Object Identifier 10.1109/ACCESS.2017.DOI

Saliency model extension for sensorless initial position and polarity detection of permanent magnet synchronous motors

ISTVÁN SZALAY[1], DÉNES FODOR[1], KRISZTIÁN ENISZ[1] AND HUNOR MEDVE[1]
[1]University of Pannonia, Veszprém, Hungary
Corresponding author: István Szalay (e-mail: szalay.istvan@mk.uni-pannon.hu).

This work was supported in part by the TKP2020-NKA-10 project financed under the 2020-4.1.1-TKP2020 Thematic Excellence Programme by the National Research, Development and Innovation Fund of Hungary, and by the ZalaZONE Automotive Proving Ground Zala Ltd. The research was supported by the Ministry of Innovation and Technology NRDI Office within the framework of the Autonomous Systems National Laboratory Program.

ABSTRACT In this paper, we propose an extended permanent magnet synchronous motor model that incorporates a quadratic flux-current function to determine the polarity-dependent saliency and develop a sensorless initial position detection method that is capable of polarity detection. The quadratic model extension is based on the second-order Taylor polynomial of the flux-current function. We present the model equations in both the stator- and the rotor-oriented reference frames as well as the Park and inverse Park transforms of the quadratic terms and Hessian matrices. The transient behavior and the dependency of the extended model on the rotor position have been validated. The proposed initial position detection method injects non-modulated even square wave voltage signals and relies only on phase-current measurements. We analyzed the effect of the pulse length on the errors of the position estimation and polarity detection. We provide machine parameter-based approximations of the current components dependent on the rotor position and, based on them, present a quantitative pulse-length design method.

INDEX TERMS Sensorless electric drives, saliency modeling, initial position detection, polarity detection.

I. INTRODUCTION

THE ever increasing industrial requirements in terms of performance and efficiency have led to the adoption of synchronous machines in a wide variety of applications ranging from home appliances to electric vehicles [1]–[4]. Permanent magnet synchronous motors (PMSMs) are attractive candidates for high-performance applications because of their high power density, high efficiency and high torque-to-volume ratio as well as their suitability for constant power operation over a wide speed range [5]. The motion control of the PMSM drives is based on current and rotor position feedback, where the latter is necessary to maintain an appropriate space angle between the stator and rotor fields [6]. To start the motor without any unwanted vibrations and reverse rotation, it is also necessary to determine the initial rotor position [7].

Conventional PMSM drives utilize a shaft-mounted optical encoder or a resolver to determine the rotor position. In many industrial installations, the presence of the shaft sensor may substantially reduce the overall ruggedness of the drive; in others, it may add significantly to the cost and size of the drive [8]–[10]. To design a more robust, cost-effective and, therefore, more competitive PMSM drive system, it is key to eliminate shaft-mounted sensors as well as related electronics and wiring by introducing position-sensorless control schemes. Furthermore, many rotor position sensors provide the initial rotor position with an inadequate resolution and incremental encoders do not provide it at all.

A. POSITION-SENSORLESS METHODS

Sensorless methods for PMSMs determine the rotor position in terms of electrical angle without a mechanical position sensor usually based on phase current measurements and a suitable machine model. Sensorless control techniques that rely on the fundamental excitation model are capable of providing high-performance control above about 3 % of the nominal speed when the back electromotive force (back-EMF) is sufficiently large [10]–[16].

Sensorless methods proposed for use at lower speeds and standstill, are generally based on inductance variation due to geometrical and saturation effects [17], [18]. These techniques exploit the anisotropic properties of PM machines, caused by the saliency of an interior permanent magnet rotor and/or the saturation of the iron cores.

The anisotropy tracking techniques are either based on fundamental pulse-width modulation excitation (FPE) or signal injection [19], [20]. Both low-frequency and high-frequency signal injection (HFSI) methods have been developed [21], [22]. Modulated sinusoidal HFSI techniques inject a high-frequency carrier signal with a small amplitude using either a pulsating space vector in the estimated rotor reference frame or a rotating space vector in the stationary reference frame [23]–[25]. Square-wave HFSI methods inject modulated or non-modulated, continuous or intermittent signals [26]. Usually, HFSI methods are capable of tracking both geometric and saturation-caused anisotropies [12], [27].

B. INITIAL POSITION DETECTION METHODS

The zero-speed or initial position detection is performed over two steps by many methods. First, the inductance-based saliency tracker searches for the $+d/-d$ axis, then another method detects magnet polarity [12], [28], [29]. Both steps require high-frequency models which are often derived from the corresponding fundamental frequency models [11].

The critical part of the high-frequency machine models is the saliency model which describes the dependency of the electrical parameters on the rotor position such as self and mutual inductances as well as the non-linearities related to magnetic saturation. Some papers classify these as primary and secondary saliencies [30], [31]. In most PMSMs, the primary saliency is present in the inductances. The abc self and mutual inductances have a dominant second spatial harmonic in terms of the electrical angle, and the L_d and L_q inductances are different constants [32]. Although saliency tracking can use the primary saliency to identify the $+d/-d$ axis, the polarity of the rotor's magnets cannot be determined based on them because the abc inductance values at any ϑ and $\vartheta+180°$ electrical rotor positions are equal. Given that this ambiguity may cause reverse rotation and unwanted oscillation, another method is needed to determine the polarity.

C. POLARITY DETECTION

To determine magnet polarity, it is possible to exploit secondary saliencies that have significant first spatial harmonics. Many papers introduce the injection of short voltage pulses to determine the polarity after identifying the $+d/-d$ axis [12], [33]. Experimental results show that a voltage pulse in the $+d$ or magnetizing direction has a higher response current than a voltage pulse of the same amplitude and duration in the $-d$ or demagnetizing direction, due to the nonlinearity of magnetic saturation [34]–[36]. Some solutions exploit this nonlinear behavior using multiple voltage pulses to directly determine the rotor position without using an inductance-based d-axis tracking technique [26], [36], [37].

While the primary saliency can be modeled as a linear relation between the flux-linkages and the current, the secondary, polarity-dependent saliency is non-linear with respect to the phase currents. Related papers describe various approaches for modeling it. Some papers define different L_d fractional inductance values for positive and negative currents that have the opposite values at the north and south poles [26], [33], [36], [38]–[40]. This approach uses two linear systems of different time-constants and the resulting model is limited to the d direction. Other papers develop signal processing methods to extract the polarity information from the second harmonic content of the current vector [30], [41].

A more general approach is to formulate the flux-current relations as Taylor polynomials of the underlying non-linear functions. Reference [5] formulates the d direction flux-linkage (Ψ_d) as a quadratic function of the d direction current (i_d) using the constant, linear, and quadratic terms of the Taylor polynomial. In this approach, the coefficient of the quadratic term (the second derivative of Ψ_d with respect to i_d) holds the polarity information. References [41] and [42] formulate i_d as a quadratic function of Ψ_d and the polarity-dependent quantity is the second derivative of i_d with respect to Ψ_d. Reference [34] expresses L_d and L_q as quadratic functions of i_d and i_q, respectively. Here the coefficient of the d direction linear term is polarity-dependent. The polarity-dependent quantity is always related to the curvature of the d direction magnetization curve. High-frequency models usually neglect the phase resistances [11], [12], [40], [43].

D. CONTRIBUTIONS

In this paper, a novel extended PMSM model is proposed which includes a quadratic flux-current function to represent the polarity-dependent saliency. Based on the model, a sensorless initial position detection method was developed which is capable of polarity-detection. The first part of the paper, Sections II–VI, describes the proposed model and presents measurement data for the elements of the inductance and Hessian matrices. The second part, Sections VII–IX, validates the model and presents a voltage pulse injection-based initial position and polarity detection method.

The main contributions of this paper are:

- A novel extended PMSM model is proposed that integrates the polarity-dependent saliency into the traditional machine modeling framework. Park and inverse Park transforms for both the extended voltage equation and Hessian matrices have been derived;
- A parameter identification method based on a specific measurement protocol is presented for the elements of the abc Hessian matrix;
- The proposed model is able to explain the difference between the current response to a positive and to a negative voltage pulse. It also correctly predicts the transient behavior and rotor position dependence of the current differences caused by the polarity-dependent saliency;
- A voltage pulse injection-based initial position detection method is presented that requires only phase current measurements and causes no rotor movement;
- A pulse-length selection method is also presented for designing a reliable polarity detection algorithm.

TABLE 1. Nomenclature.

Symbol	Description	Symbol	Description
U_{DC}	DC-link voltage	R	Phase resistance
L_{sl}	Leakage inductance	$L_{s\sigma}$	Magnetizing inductance
z_P	Number of pole-pairs	$\otimes$	Kronecker product

Symbol	Description
$\underline{T}(\vartheta)$ and $\underline{T}^{-1}(\vartheta)$	Park and inverse Park transformation matrices
$\underline{u}_{abc}$ and $\underline{u}_{dq0}$	Voltage vector in abc and $dq0$
$\underline{i}_{abc}$ and $\underline{i}_{dq0}$	Current vector in abc and $dq0$
$\underline{\Psi}_{abc}$ and $\underline{\Psi}_{dq0}$	Flux-linkage vector in abc and $dq0$
$\underline{\Psi}^{PM}_{abc}$ and $\underline{\Psi}^{PM}_{dq0}$	Permanent magnet flux-linkage vector in abc/$dq0$
$\underline{\underline{J}}^{f}_{\underline{x}_0}$	Jacobian of f evaluated at $\underline{x}_0$
$\underline{\underline{H}}^{f}_{\underline{x}_0}$	Hessian of f evaluated at $\underline{x}_0$
$\underline{\underline{L}}_{abc}(\vartheta)$ and $\underline{\underline{L}}_{dq0}$	Differential inductance matrices in abc and $dq0$
L_x	Amplitude of the second spatial harmonics of the abc inductances
$L_{\min}$, $L_{\max}$	Minimum and maximum self-inductances in abc
$\underline{\Gamma}_k(\vartheta)$	Hessian of the flux-linkage of phase $k\in\{a,b,c\}$
$\underline{\Gamma}_{abc}(\vartheta)$ and $\underline{\Gamma}_{dq0}$	Combined and flattened Hessian of the three-phase flux-linkage function in abc and $dq0$
Γ_0	Polarity-dependent saliency coefficient
$_{gpn}$ and ^{G}	Generalized indexing subscripts and superscripts
i^G_g, i^G_p, i^G_n	Phase mean currents
Δi^G_g, Δi^G_p, Δi^G_n	Phase current differences
i^G and Δi^G	Combined mean currents and current differences
ϑ and $\hat{\vartheta}$	True and estimated electrical rotor positions
$\Delta\vartheta$	Electrical rotor position estimation error
$P^{U_{DC}}_{\alpha}$	Probability of correct polarity detection
$f\|_{\underline{x}_0}$	Notation for function f evaluated at $\underline{x}_0$

II. EXTENDED THREE-PHASE MACHINE MODEL

The mathematical model of a PMSM used in control design can be divided into three main parts: the electrical, the magnetic and the mechanical model. The electrical model is expressed in the form of the phase voltage equations. The magnetic model contains the saliency model and describes the relationship between the flux-linkages, the phase currents and the rotor position. The mechanical model consists of the torque equation of the rotor. In the development of a sensorless method for standstill, the first two are more significant.

The phase voltage equations can be written as a system of differential equations or a shorter single differential equation of vector-valued functions. Equation (2) is the vectorial form in the stator-oriented three-phase reference frame [44].

$$\begin{bmatrix} u_a \\ u_b \\ u_c \end{bmatrix} = R \begin{bmatrix} i_a \\ i_b \\ i_c \end{bmatrix} + \frac{\mathrm{d}}{\mathrm{d}t} \begin{bmatrix} \Psi_a \\ \Psi_b \\ \Psi_c \end{bmatrix} \tag{1}$$

$$\underline{u}_{abc} = R\underline{i}_{abc} + \frac{\mathrm{d}\underline{\Psi}_{abc}}{\mathrm{d}t} \tag{2}$$

The phase resistance was taken into consideration.

A. LINEARIZED FLUX MODEL

In the general case, there is a non-linear and hysteretic relationship between the flux-linkages, phase currents and the rotor position. In order to formulate the flux-linkage vector $\underline{\Psi}_{abc}$ as a function of the phase currents and the rotor position, the effect of hysteresis is neglected. Although the $\underline{\Psi}_{abc}(\underline{i}_{abc},\vartheta)$ function shows nonlinear properties, the traditional approach is linearization, the machine models only include the constant and linear terms of the Taylor series expansion, while the higher order terms are omitted.

The Taylor series expansion of the flux-linkage function is performed with respect to the phase current vector $\underline{i}_{abc}$, around the ($\underline{i}_{abc}=\underline{0}\,\mathrm{A},\vartheta$) point, which means no phase currents are present and the electrical rotor position is fixed to ϑ. The result is (3), a polynomial approximation with rotor position-dependent coefficients.

$$\underline{\Psi}_{abc}(\underline{i}_{abc},\vartheta) = \underline{\Psi}_{abc}(\underline{0}\,\mathrm{A},\vartheta) + \underline{\underline{J}}^{\underline{\Psi}_{abc}}_{(\underline{0}\,\mathrm{A},\vartheta)}\underline{i}_{abc} + \ldots \tag{3}$$

The constant coefficient vector is equal to the flux-linkage vector of the permanent magnets, $\underline{\Psi}^{PM}_{abc}$. It is important to note that although it is constant with respect to the phase currents, its value depends on the rotor position.

$$\underline{\Psi}^{PM}_{abc}(\vartheta) = \underline{\Psi}_{abc}(\underline{0}\,\mathrm{A},\vartheta) \tag{4}$$

The coefficient matrix of the linear term is the Jacobian of $\underline{\Psi}_{abc}$ and is equal to the differential inductance matrix, $\underline{\underline{L}}_{abc}$.

$$\underline{\underline{L}}_{abc}(\vartheta) = \underline{\underline{J}}^{\underline{\Psi}_{abc}}_{(\underline{0}\,\mathrm{A},\vartheta)} = \left.\frac{\partial\underline{\Psi}_{abc}}{\partial\underline{i}_{abc}}\right|_{(\underline{0}\,\mathrm{A},\vartheta)} \tag{5}$$

The traditionally used linearized form of the flux-linkage function only contains the constant and linear terms.

$$\underline{\Psi}_{abc}(\underline{i}_{abc},\vartheta) = \underline{\Psi}^{PM}_{abc}(\vartheta) + \underline{\underline{L}}_{abc}(\vartheta)\,\underline{i}_{abc} \tag{6}$$

The components of the permanent magnet flux-linkage vector $\underline{\Psi}^{PM}_{abc}$ have dominant fundamental spatial harmonics in electrical angle, while their mean value and higher harmonics are negligible. In PM machines, the flux of the permanent magnets is dominant and the current-induced flux is usually much lower. The overall magnetization state of the iron parts is determined by the rotor position and the current-induced flux can only change the magnetization state slightly. At a standstill, the magnetization state and the corresponding magnetization curve depend on the rotor position as shown for phase a in Fig. 1.

The $\Psi_a(i_a)$ magnetization curve has different vertical intercepts, gradients and curvatures at different rotor positions. The vertical intercept corresponds to the permanent magnet flux in phase a. The gradient of the magnetization curve is the self-inductance of phase a, namely L_{aa}. During an electrical revolution, the self-inductance is always positive and has a minimum in the $+d$ direction (north pole), a maximum in the $+q$ direction, a second minimum in $-d$ direction (south pole) and a second maximum in the $-q$ direction, see Figs. 1–3. L_{aa} has a non-zero mean value and a dominant second spatial harmonic in electrical angles. Self- and mutual inductances all have second spatial harmonics with different phase offsets.

B. LIMITATION OF THE LINEARIZED FLUX MODEL

In the voltage equation (2), we can see the time derivative of the flux-linkage. This means that the flux-linkages only have an effect on the currents when their values change. At a standstill, the rotor position and the flux-linkages of the permanent magnets are constant so have no effect on the phase currents. Therefore, only the inductances have a position-dependent effect on the currents, and that involves their second spatial harmonics (see L_{aa} in Fig. 3). The second spatial harmonics consist of two periods during an electrical revolution and therefore

$$\underline{L}_{abc}(\vartheta) = \underline{L}_{abc}(\vartheta+180°)\,. \tag{7}$$

Hence, the inductance-based anisotropy tracking methods always yield an ambiguity of 180° in electrical angle [28], [45], [46]. In light of the above, the linearized flux model (6) is unsuitable for polarity detection.

C. QUADRATIC FLUX MODEL EXTENSION

To overcome the limitation of the linearized flux-linkage model, we extended it with the quadratic term of the Taylor series expansion by generalizing the non-linear modeling approaches [5], [34], [42]. The coefficients of the quadratic term contain the second derivatives of the flux-linkages with respect to the phase currents. The second derivatives correspond to the curvature of the magnetization curve. The exact form of the flux-linkage function is unknown.

Based on the fact that the self-inductances of the phases are smaller when the absolute value of the flux-linkages of the permanent magnets is larger, we hypothesized, that the flux-linkage components are sigmoid (S-shaped) functions. In the case of phase a, as shown in Fig. 1, the curvature of $\Psi_a(i_a)$ is negative when the phase winding is closer to the north pole and positive when closer to the south pole. This leads to a zero mean value and a dominant first spatial harmonic in electrical angle, as shown in Fig. 3.

The quadratic coefficient matrix contains the 3×3 Hessians of the three phase flux-linkages and has 3×3×3 elements in total, therefore, appears to be a three-dimensional matrix or a third-order tensor. To avoid the three-dimensional forms and tensor formalism, we decided to combine and flatten the Hessians into a 9×3 two-dimensional matrix by rearranging the 3×3 Hessians of the phase flux-linkages below each other. The Hessian of the flux-linkage of phase $k\in\{a,b,c\}$ is the symmetric matrix

$$\underline{\Gamma}_k(\vartheta) = \underline{\underline{H}}^{\Psi_k}_{(\underline{0}\,\mathrm{A},\vartheta)} = \left.\frac{\partial^2\Psi_k}{\partial\underline{i}^2_{abc}}\right|_{(\underline{0}\,\mathrm{A},\vartheta)} \in \mathbb{R}^{3\times3}. \tag{8}$$

The combined and flattened Hessian of the three-phase flux-linkage function is

$$\underline{\Gamma}_{abc}(\vartheta) = \underline{\underline{H}}^{\underline{\Psi}_{abc}}_{(\underline{0}\,\mathrm{A},\vartheta)} = \begin{bmatrix} \underline{\Gamma}_a(\vartheta) \\ \underline{\Gamma}_b(\vartheta) \\ \underline{\Gamma}_c(\vartheta) \end{bmatrix} \in \mathbb{R}^{9\times3}. \tag{9}$$

To make the notation shorter, we used the capital letter Γ to denote the Hessian matrices and their elements.

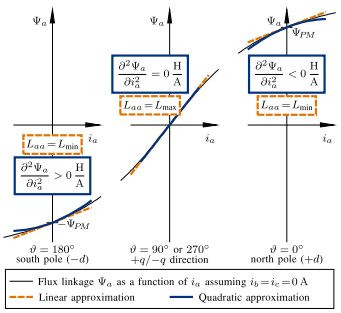

FIGURE 1. The flux-linkage Ψ_a and it's linear and quadratic approximations at significant rotor positions. The quadratic approximation contains information about the polarity of the rotor magnets while the linear equivalent does not.

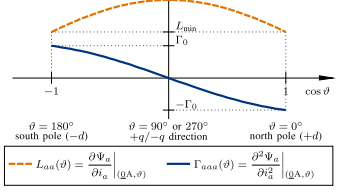

FIGURE 2. The first and second derivatives of the flux-linkage Ψ_a with respect to i_a evaluated at ($\underline{0}\,\mathrm{A},\vartheta$) that define $L_{aa}(\vartheta)$ and $\Gamma_{aaa}(\vartheta)$.

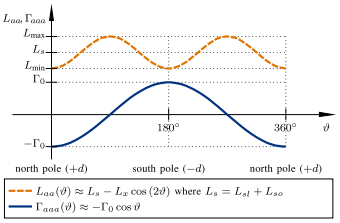

FIGURE 3. The first and second derivatives of the flux-linkage Ψ_a evaluated at ($\underline{0}\,\mathrm{A},\vartheta$) and plotted as functions of the electrical rotor position.

The quadratic approximation of the three-phase flux-linkage function that incorporates the flattened Hessian is

$$\underline{\Psi}^{PM}_{abc}(\vartheta) + \underline{L}_{abc}(\vartheta)\,\underline{i}_{abc} + \frac{1}{2}\left(\underline{I}_3 \otimes \underline{i}^T_{abc}\right)\underline{\Gamma}_{abc}(\vartheta)\,\underline{i}_{abc}, \quad (10)$$

where the constant term refers to the flux-linkage of the permanent magnets, the linear term stands for the matrix product of the inductance matrix and the current vector, and the quadratic term represents the effect of the curvature of the magnetization curves. $\otimes$ denotes the Kronecker product.

D. THE VOLTAGE EQUATION AT A STANDSTILL

The voltage equation of our three-phase star-connected PMSMs at a standstill takes the form of (11) after substituting the quadratic flux-linkage (10) into the voltage equation (2).

$$\underline{u}_{abc} = R\underline{i}_{abc} + \underline{L}_{abc}(\vartheta)\frac{\mathrm{d}\underline{i}_{abc}}{\mathrm{d}t} + \left(\underline{I}_3 \otimes \underline{i}^T_{abc}\right)\underline{\Gamma}_{abc}(\vartheta)\frac{\mathrm{d}\underline{i}_{abc}}{\mathrm{d}t} \quad (11)$$

For an ideal machine that has identical phase windings, the three-phase voltage equation (11) contains 9 unknown inductances and 18 unknown elements in the abc Hessian, $\underline{\Gamma}_{abc}$, defined in (9), that are all functions of the rotor position.

The inductive and quadratic terms of (11) can be rearranged to reveal that the quadratic flux-linkage model is equivalent to a seemingly linear model which in fact have a current-dependent inductance matrix.

$$\underline{u}_{abc} = R\underline{i}_{abc} + \underbrace{\left(\underline{L}_{abc}(\vartheta) + \left(\underline{I}_3 \otimes \underline{i}^T_{abc}\right)\underline{\Gamma}_{abc}(\vartheta)\right)}_{\underline{L}^{\mathrm{cdi}}_{abc}(\underline{i}_{abc},\vartheta)}\frac{\mathrm{d}\underline{i}_{abc}}{\mathrm{d}t} \quad (12)$$

Here, $\underline{L}^{\mathrm{cdi}}_{abc}(\underline{i}_{abc},\vartheta)$ is the current-dependent abc inductance matrix which is a linear function of the $\underline{i}_{abc}$ current vector. Its constant term is the differential inductance matrix $\underline{L}_{abc}$ and the coefficient matrix of its linear term is the Hessian $\underline{\Gamma}_{abc}$. We point out this connection because the existing modeling approaches usually define the inductances to be current dependent instead of extending directly the flux-linkage [17], [47], [48].

III. MEASURING THE ROTOR POSITION DEPENDENCE OF THE MACHINE PARAMETERS

We designed and built a measurement environment to identify the rotor position dependence of the unknown inductances and Hessian coefficients of our test motors as well as to implement a sensorless initial position detection method. When performing measurements on a star-connected motor with all three terminals connected to the inverter, only certain combinations of the machine parameters can be determined. To make all three-phase parameters obtainable, we modified our test motors and made their neutral points accessible. This modification enabled the independent control and measurement of the phase voltages and currents as well as the implementation of both single- and two-phase measurements. The schematic diagram of the measurement environment can be seen in Fig. 6.

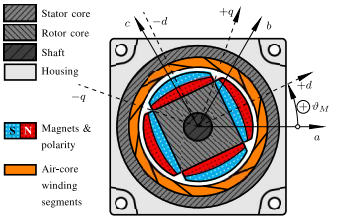

FIGURE 4. The cross-section and main components of the Maxon EC4-pole 45 252463, the two pole-pairs slotless PMSM used in our experimental drive.

TABLE 2. Datasheet parameters of the Maxon EC4-pole 45 252463 type.

Parameter	Value
Nominal voltage	48 V
Nominal speed	6120/min
Stall torque	4070 mN m
Starting current	54.7 A
No load current	261 mA
Maximum continuous current	4.16 A
Terminal-to-terminal resistance	878 mΩ
Terminal-to-terminal inductance	350 µH
Torque constant	74.5 mN m/A
Rotor inertia	200 g cm²
Mechnical time constant	3.16 ms
Number of pole-pairs	2

A. TEST MOTORS

We used two Maxon EC4-pole 45 252463 slotless PMSMs as our test motors. Table 2 contains the datasheet parameters and Fig. 4 shows the cross-section of the test motors.

Factory-mounted optical encoders of 13-bit resolution are installed on the test motors. The size of the encoder module is comparable to the size of the motor itself.

B. MEASUREMENT AUTOMATION

The unknown inductances and Hessians are rotor position dependent and their values have to be identified at various rotor positions. Therefore, we designed our measurement system to be able to automatically change the rotor position using a stepper motor with a resolution of 0.9° which is equivalent to a resolution of 1.8° in terms of electrical angle for our two pole-pair test motors. We used the factory-mounted encoders to correct the position error introduced by the stepper motor.

We implemented the drive control on a National Instruments CompactRIO. The low-level functions, e.g. MOSFET control signal generation, current sampling, encoder signal processing and data acquisition, run on the cRIO-9104 FPGA module. The FPGA stores the measured current and rotor position values in the FIFO memory of the cRIO-9104 real-time controller which streams the current and position data to our LabVIEW-based control application.

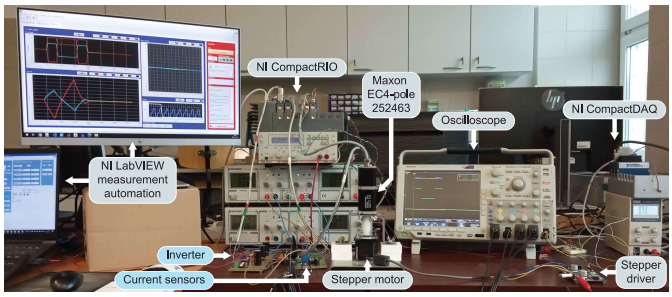

FIGURE 5. The photo of our experimental PMSM drive and measurement environment.

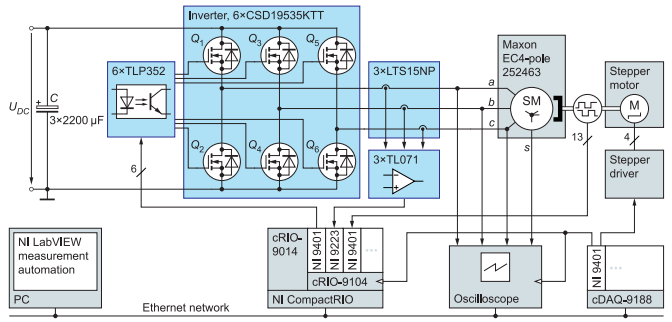

FIGURE 6. The schematics of our experimental PMSM drive and measurement environment.

We decided to measure the phase voltages and the neutral point voltage using a Tektronix MSO 4054B oscilloscope. We used a CompactDAQ cDAQ-9188 as the digital output to control the stepper driver as well as trigger the injection and the oscilloscope measurement. The external triggering of the FPGA and the oscilloscope eliminated the latency introduced by the Ethernet network we used to connect the instruments. It was very important to synchronize the operation of the FPGA and the oscilloscope because the time series-based parameter-identification method we used requires synchronized voltage and current data. We performed the voltage measurement at a higher sampling frequency in order to capture the switching transients and downsampled the voltage data to match the sampling time of the current data.

Fig. 5 shows a photo of the experimental PMSM drive and measurement environment. Fig. 6 shows the schematics of the system. Our custom-designed and built parts include the three-phase inverter, optical coupling, current measurement and amplification circuits. They are represented by blue labels in Fig. 5 and by blue blocks in Figs. 6 and 7. The types of their components are also shown.

On Fig. 5 the oscilloscope screen shows the measured terminal voltages while the measured phase voltages and currents are visible on the computer screen.

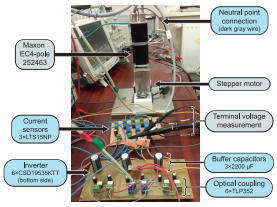

FIGURE 7. The photo of the custom-designed experimental PMSM drive.

IV. FLUX MODEL PARAMETER IDENTIFICATION

The structure of the voltage equation (11) in the cases of single- and two-phase excitation schemes permits the use of the linear least squares method to identify the model parameters from time series data of phase voltages and currents. The following sections present the specific variants of the voltage equation and parameter identification methods used for single- and two-phase measurements.

A. MEASUREMENTS AND IDENTIFICATION USING SINGLE PHASE EXCITATION

In a single-phase excitation measurement, we connected only one of the phase terminals and the neutral point to two inverter legs. Fig. 8 shows the single-phase excitation arrangement for phase a. The single-phase excitation in the case of phase a prohibits the current to flow in phases b and c. The phase voltage equations that apply can be derived from the three-phase equation (11) by substituting $i_b = i_c = 0$ A.

$$u_a = u_{a0} - u_s = R_a i_a + L_{aa}(\vartheta)\frac{\mathrm{d}i_a}{\mathrm{d}t} + \frac{1}{2}\Gamma_{aaa}(\vartheta)\frac{\mathrm{d}i_a^2}{\mathrm{d}t} \quad (13)$$

$$u_b = u_{b0} - u_s = L_{ba}(\vartheta)\frac{\mathrm{d}i_a}{\mathrm{d}t} + \frac{1}{2}\Gamma_{baa}(\vartheta)\frac{\mathrm{d}i_a^2}{\mathrm{d}t} \quad (14)$$

$$u_c = u_{c0} - u_s = L_{ca}(\vartheta)\frac{\mathrm{d}i_a}{\mathrm{d}t} + \frac{1}{2}\Gamma_{caa}(\vartheta)\frac{\mathrm{d}i_a^2}{\mathrm{d}t} \quad (15)$$

The phase voltages u_a, u_b and u_c are equal to the differences between the terminal voltages and the voltage of the star point u_s. The voltage equation of the excited phase a (13) contains the resistive voltage drop and the derivative of the phase flux which provides the linear and quadratic terms. These terms encompass all the dynamics of a single phase. The other two equations describe the interactions between the current of the excited phase and the non-excited phases as well as contain only induced voltages. However, these equations do not contain all the elements of the Hessian matrix. To overcome this problem, two-phase excitation measurements were subsequently performed.

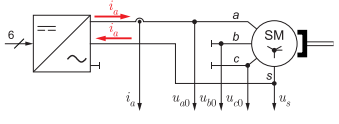

FIGURE 8. Single-phase excitation arrangement for measurement of phase a where g=a, p=b, n=c, and i_b=i_c=0 A, realized using the neutral point s.

TABLE 3. Generalized phase indexing.

g Reference	p +120° (electrical)	n −120° (electrical)
a	b	c
b	c	a
c	a	b

We applied a generalized phase indexing where g denotes the excited or reference phase, p denotes the phase at +120° and n denotes the phase at −120° (see Table 3).

Using generalized indices, where g, p and n can be a, b, and c, respectively, according to Table 3:

$$u_g = R_g i_g + L_{gg}(\vartheta)\frac{\mathrm{d}i_g}{\mathrm{d}t} + \frac{1}{2}\Gamma_{ggg}(\vartheta)\frac{\mathrm{d}i_g^2}{\mathrm{d}t} \quad (16)$$

$$u_p = L_{pg}(\vartheta)\frac{\mathrm{d}i_g}{\mathrm{d}t} + \frac{1}{2}\Gamma_{pgg}(\vartheta)\frac{\mathrm{d}i_g^2}{\mathrm{d}t} \quad (17)$$

$$u_n = L_{ng}(\vartheta)\frac{\mathrm{d}i_g}{\mathrm{d}t} + \frac{1}{2}\Gamma_{ngg}(\vartheta)\frac{\mathrm{d}i_g^2}{\mathrm{d}t} \quad (18)$$

Parameter identification uses the time series created by sampling the voltages and the excitation current:

$$u_{g,k} = u_g(kT_S), \quad \underline{u}_g = \left[u_{g,1} \dots u_{g,N}\right]^T \quad (19)$$

$$i_{g,k} = i_g(kT_S), \quad \underline{i}_g = \left[i_{g,1} \dots i_{g,N}\right]^T \quad (20)$$

$$u_{p,k} = u_p(kT_S), \quad \underline{u}_p = \left[u_{p,1} \dots u_{p,N}\right]^T \quad (21)$$

$$u_{n,k} = u_n(kT_S), \quad \underline{u}_n = \left[u_{n,1} \dots u_{n,N}\right]^T \quad (22)$$

We calculated the derivative of the excitation current (d) and the derivative of the square of the excitation current (q) using the following central differencing formulae:

$$d_{g,k} = \frac{i_{g,k+1} - i_{g,k-1}}{2T_S}, \quad \underline{d}_g = \left[d_{g,1} \dots d_{g,N}\right]^T \quad (23)$$

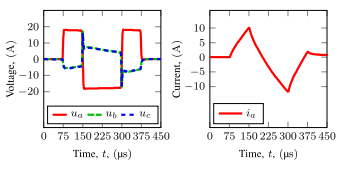

FIGURE 9. Signals acquired during the single-phase excitation of phase a, starting with a rising edge, at electrical rotor position $\vartheta = 0°$.

$$q_{g,k} = \frac{i^2_{g,k+1} - i^2_{g,k-1}}{2T_S}, \quad \underline{q}_g = \left[q_{g,1} \dots q_{g,N}\right]^T \quad (24)$$

The time series forms of the voltage equations are

$$\underline{u}_g = R_g\underline{i}_g + L_{gg}(\vartheta)\,\underline{d}_g + \frac{1}{2}\Gamma_{ggg}(\vartheta)\,\underline{q}_g, \quad (25)$$

$$\underline{u}_p = L_{pg}(\vartheta)\,\underline{d}_g + \frac{1}{2}\Gamma_{pgg}(\vartheta)\,\underline{q}_g \text{ and} \quad (26)$$

$$\underline{u}_n = L_{gg}(\vartheta)\,\underline{d}_g + \frac{1}{2}\Gamma_{ngg}(\vartheta)\,\underline{q}_g. \quad (27)$$

The linear least squares method requires an equation in the form $\underline{y} = \underline{X}\,\underline{\beta}$ and solves it for $\underline{\beta}$. We rearranged the time series equations (25)–(27) into the required forms.

$$\underline{y}_g = \underline{u}_g = \begin{bmatrix}\underline{i}_g & \underline{d}_g & \frac{1}{2}\underline{q}_g\end{bmatrix}\begin{bmatrix}R_g \\ L_{gg}(\vartheta) \\ \Gamma_{ggg}(\vartheta)\end{bmatrix} = \underline{X}_g\underline{\beta}_g \quad (28)$$

$$\underline{y}_p = \underline{u}_p = \begin{bmatrix}\underline{d}_g & \frac{1}{2}\underline{q}_g\end{bmatrix}\begin{bmatrix}L_{pg}(\vartheta) \\ \Gamma_{pgg}(\vartheta)\end{bmatrix} = \underline{X}_p\underline{\beta}_p \quad (29)$$

$$\underline{y}_n = \underline{u}_n = \begin{bmatrix}\underline{d}_g & \frac{1}{2}\underline{q}_g\end{bmatrix}\begin{bmatrix}L_{ng}(\vartheta) \\ \Gamma_{ngg}(\vartheta)\end{bmatrix} = \underline{X}_n\underline{\beta}_n \quad (30)$$

In a single measurement, we injected a single period of a bipolar even square wave voltage signal. The injected voltage, the induced voltages in the other two phases and the current response are shown in Fig. 9. Using the data produced by a single-phase measurement, we were able to identify the value of 3×7 parameters for a specified ϑ rotor position, namely 3 phase resistances, 3 self-inductances, 6 mutual inductances, and 9 diagonal elements of the Hessian.

B. MEASUREMENTS AND IDENTIFICATION USING TWO-PHASE EXCITATION

In our two-phase measurements, we excited two phases, namely g and p connected in series (see Fig. 10). The two phase currents have opposite signs, i.e. i_p is equal to $-i_g$. In the voltage equations of the two-phase measurements, the coefficients are the linear combinations of certain elements of the inductance and Hessian matrices.

The combined coefficients of the voltage equation of phase g are

$$\Sigma L_g(\vartheta) = L_{gg}(\vartheta) - L_{gp}(\vartheta) \text{ and} \quad (31)$$

$$\Sigma\Gamma_g(\vartheta) = \Gamma_{ggg}(\vartheta) - 2\Gamma_{ggp}(\vartheta) + \Gamma_{gpp}(\vartheta)\,. \quad (32)$$

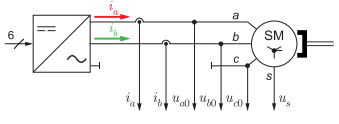

FIGURE 10. Two-phase excitation arrangement for measurement of phases a and b where g=a, p=b, n=c, i_b=$-i_a$ and i_c=0 A.

The combined coefficients of the voltage equation of phase p are

$$\Sigma L_p(\vartheta) = L_{pg}(\vartheta) - L_{pp}(\vartheta) \text{ and} \quad (33)$$

$$\Sigma\Gamma_p(\vartheta) = \Gamma_{pgg}(\vartheta) - 2\Gamma_{pgp}(\vartheta) + \Gamma_{gpp}(\vartheta)\,. \quad (34)$$

The combined coefficients of the voltage equation of phase n are

$$\Sigma L_n(\vartheta) = L_{ng}(\vartheta) - L_{np}(\vartheta) \text{ and} \quad (35)$$

$$\Sigma\Gamma_n(\vartheta) = \Gamma_{ngg}(\vartheta) - 2\Gamma_{ngp}(\vartheta) + \Gamma_{npp}(\vartheta)\,. \quad (36)$$

The voltage equations using the combined coefficients are

$$\underline{u}_g = R_g\underline{i}_g + \Sigma L_g(\vartheta)\,\underline{d}_g + \frac{1}{2}\Sigma\Gamma_g(\vartheta)\,\underline{q}_g, \quad (37)$$

$$\underline{u}_p = R_p\underline{i}_p + \Sigma L_p(\vartheta)\,\underline{d}_g + \frac{1}{2}\Sigma\Gamma_p(\vartheta)\,\underline{q}_g \text{ and} \quad (38)$$

$$\underline{u}_n = \Sigma L_n(\vartheta)\,\underline{d}_g + \frac{1}{2}\Sigma\Gamma_n(\vartheta)\,\underline{q}_g. \quad (39)$$

Using the data produced by a two-phase measurement, we were able to identify the values of the non-diagonal elements Γ_{ggp}, Γ_{pgp} and Γ_{ngp} of the Hessian matrix as a function of the ϑ electrical rotor position.

V. MEASUREMENT RESULTS

We set the DC supply voltage to 18 V and 36 V for the single- and two-phase measurements, respectively, to ensure that the phase currents will have similar peak values. The injected bipolar even square wave voltage signal was composed of three sections: 75 µs in the reference direction, 2×75 µs in the opposite direction, and 75 µs in the reference direction again, as shown in Fig. 9 for phase a and in the positive reference direction. The current response is almost symmetric, has a time integral close to zero and produces a negligibly small net change in the angular momentum of the rotor, or in other words, the the rotor does not move. Using a 4×75 µs-long injection, the peak current values were around ±10-12 A or 20-25 % of the starting current. The measurements produced 400 data points during a full mechanical rotation leading to a resolution of 1.8° in electrical angle.

A. THE IDENTIFIED INDUCTANCE VALUES

The identified self-inductances are shown in Fig. 11. They have non-zero average values and dominant second spatial harmonics. We fitted the idealized curves (40)–(42) to the measured data. The average value of the self-inductances is equal to $L_{sl} + L_{so}$, where L_{sl} denotes the leakage inductance and L_{so} stands for the magnetizing inductance. The amplitude of the second spatial harmonic is denoted by L_x. The spatial phase offset between the self-inductances is 120°.

$$L_{aa}(\vartheta) = L_{sl} + L_{so} - L_x\cos(2\vartheta) \quad (40)$$

$$L_{bb}(\vartheta) = L_{sl} + L_{so} - L_x\cos(2\vartheta + 120°) \quad (41)$$

$$L_{cc}(\vartheta) = L_{sl} + L_{so} - L_x\cos(2\vartheta + 240°) \quad (42)$$

The self-inductances are minimal at rotor positions where one of the poles (+d or −d axis) is aligned with the phase

and are at their maxima where the $+q$ or $-q$ axis is aligned with the phase. This is consistent with Figs. 1–3.

The identified mutual inductances are shown in Figs. 12 and 13. The mutual inductances, similarly to the self-inductances, have non-zero average values and dominant second spatial harmonics. The average value of the idealized mutual inductances is equal to half of $-L_{so}$ and the amplitude of the second spatial harmonic is denoted by L_x.

$$L_{ab}(\vartheta) = L_{ba}(\vartheta) = -\frac{1}{2}L_{so} - L_x\cos(2\vartheta + 240^\circ) \quad (43)$$

$$L_{bc}(\vartheta) = L_{cb}(\vartheta) = -\frac{1}{2}L_{so} - L_x\cos(2\vartheta) \quad (44)$$

$$L_{ca}(\vartheta) = L_{ac}(\vartheta) = -\frac{1}{2}L_{so} - L_x\cos(2\vartheta + 120^\circ) \quad (45)$$

Table 4 lists the fitted inductance parameters.

TABLE 4. The inductance parameters fitted to the abc inductances.

Parameter name	Notation	Value
Magnetizing inductance	L_{so}	89.17 µH
Leakage inductance	L_{sl}	31.88 µH
Inductance amplitude	L_x	15.02 µH

B. PARK TRANSFORM OF THE INDUCTANCE MATRIX

The Park transform of the inductance matrix is

$$\underline{L}_{dq0} = \underline{T}(\vartheta)\,\underline{L}_{abc}(\vartheta)\,\underline{T}^{-1}(\vartheta), \quad (46)$$

where $\underline{T}(\vartheta)$ denotes the non-power-invariant Park or direct-quadrature-zero transformation matrix, which is equal to

$$\frac{2}{3}\begin{bmatrix} \cos(\vartheta) & \cos(\vartheta-120^\circ) & \cos(\vartheta-240^\circ) \\ -\sin(\vartheta) & -\sin(\vartheta-120^\circ) & -\sin(\vartheta-240^\circ) \\ \frac{1}{2} & \frac{1}{2} & \frac{1}{2} \end{bmatrix}. \quad (47)$$

By Park transforming the idealized abc inductances (40)–(45), constant non-zero self-inductances and zero mutual inductances are obtained in the $dq0$ system.

$$\underline{L}_{dq0} = \begin{bmatrix} L_{dd} & 0 & 0 \\ 0 & L_{qq} & 0 \\ 0 & 0 & L_{00} \end{bmatrix} \quad (48)$$

The idealized values of the $dq0$ self-inductances are

$$L_{dd} = L_{sl} + \frac{3}{2}(L_{so} - L_x) = 143.11\,\mu\text{H}, \quad (49)$$

$$L_{qq} = L_{sl} + \frac{3}{2}(L_{so} + L_x) = 188.16\,\mu\text{H}, \text{ and} \quad (50)$$

$$L_{00} = L_{sl} = 31.88\,\mu\text{H}. \quad (51)$$

We computed the non-idealized values of the $dq0$ inductances based on (46) and the measured data (see Fig. 14). Although the idealized and non-idealized results are consistent, the true L_{dd} and L_{qq} have a small second spatial harmonic with an amplitude of approximately 1 µH. The $dq0$ mutual inductances, namely L_{dq}, L_{qd}, L_{d0}, L_{0d}, L_{q0} and L_{0q}, have close to zero values between -3 µH and $+3$ µH which partly can be attributed to small differences between the phase windings.

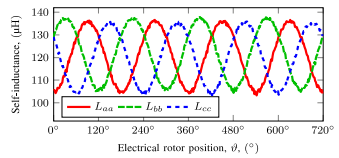

FIGURE 11. The identified L_{gg} self-inductance values calculated from 3×400 single-phase excitation measurements.

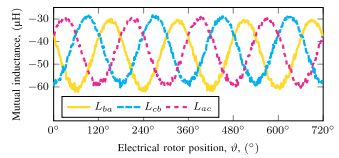

FIGURE 12. The identified L_{pg} mutual inductance values calculated from 3×400 single-phase excitation measurements.

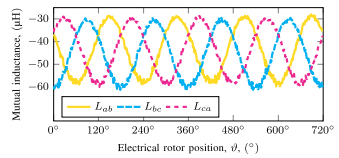

FIGURE 13. The identified L_{mg} mutual inductance values calculated from 3×400 single-phase excitation measurements.

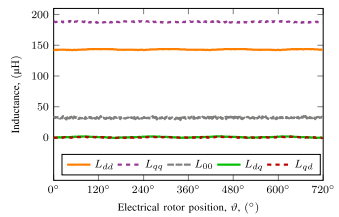

FIGURE 14. The non-idealized values of the diagonal elements of the $dq0$ inductance matrix and the non-idealized values of the $d-q$ mutual inductances calculated from 3×400 single-phase excitation measurements.

C. THE IDENTIFIED ELEMENTS OF THE HESSIAN

The single- and two-phase measurements provided enough data to identify all the elements of the abc Hessian matrix at all 400 rotor positions. The results of the parameter identification are shown in Figs. 15–20. We performed the same steps on the elements of the Hessian matrix as we took with the inductances. We fitted idealized rotor position functions to the abc elements that produce constant elements in the $dq0$ system after the Park transformation. Then we performed the transformation on both the idealized formulae and the measured data. Finally, we compared the idealized and non-idealized results in the $dq0$ system. After the examination of the measurement data, we decided to only include the first spatial harmonics in the idealized formulae of the elements of the Hessian, because 85-90 % of the signal power is produced by them. We rounded the phase offsets to multiples of 30°.

We introduced the polarity-dependent saliency coefficient Γ_0 to define the amplitudes of the main diagonal elements: Γ_{aaa}, Γ_{bbb} and Γ_{ccc}. Their measurement data are shown in Fig. 15. The main diagonal elements have close-to-zero mean values. They have negative minimum values at rotor positions where one of the north poles ($+d$ axes) is aligned with the phase and positive maximum values at the south poles ($-d$ axes). The zero crossings are located where the $+q$ or $-q$ axes are aligned with the phase. This spatial arrangement is consistent with the hypothesis that the main diagonal elements of the abc Hessian represent the curvature of the magnetization curve (see Figs. 1–3).

The idealized formulae for the main diagonal elements of the abc Hessian are

$$\Gamma_{aaa}(\vartheta) = -\Gamma_0\cos(\vartheta), \quad (52)$$

$$\Gamma_{bbb}(\vartheta) = -\Gamma_0\cos(\vartheta - 120^\circ), \text{ and} \quad (53)$$

$$\Gamma_{ccc}(\vartheta) = -\Gamma_0\cos(\vartheta - 240^\circ). \quad (54)$$

Figs. 16 and 17 show those page diagonal elements where the second and third indices are identical, but the first one is different. Similarly to the main diagonal elements, they have zero average values and a dominant first spatial harmonic in electrical angles.

We assigned the idealized formulae (55)–(60) to the page diagonal elements of the Hessian. They describe how the squares of the phase currents influence the flux in the other phases. To achieve constant elements in the $dq0$ system, we set the amplitudes of the first spatial harmonics to $\Gamma_0/\sqrt{3}$.

$$\Gamma_{baa}(\vartheta) = -\frac{\Gamma_0}{\sqrt{3}}\cos(\vartheta - 150^\circ) \quad (55)$$

$$\Gamma_{cbb}(\vartheta) = -\frac{\Gamma_0}{\sqrt{3}}\cos(\vartheta + 90^\circ) \quad (56)$$

$$\Gamma_{acc}(\vartheta) = -\frac{\Gamma_0}{\sqrt{3}}\cos(\vartheta - 30^\circ) \quad (57)$$

$$\Gamma_{abb}(\vartheta) = -\frac{\Gamma_0}{\sqrt{3}}\cos(\vartheta + 30^\circ) \quad (58)$$

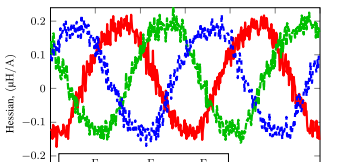

FIGURE 15. The identified main diagonal Γ_{ggg} elements of the Hessian calculated from 3×400 single-phase excitation measurements.

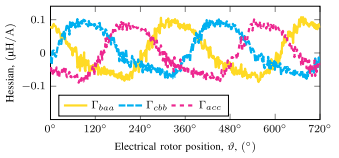

FIGURE 16. The identified page diagonal Γ_{ggg} elements of the Hessian calculated from 3×400 single-phase excitation measurements.

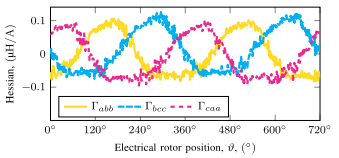

FIGURE 17. The identified page diagonal Γ_{ngg} elements of the Hessian calculated from 3×400 single-phase excitation measurements.

$$\Gamma_{bcc}(\vartheta) = -\frac{\Gamma_0}{\sqrt{3}}\cos(\vartheta - 90^\circ) \quad (59)$$

$$\Gamma_{caa}(\vartheta) = -\frac{\Gamma_0}{\sqrt{3}}\cos(\vartheta + 150^\circ) \quad (60)$$

Figs. 18 and 19 show those non-diagonal elements of the abc Hessian where the first and second indices are identical. We decided to include only the first spatial harmonics in the idealized formulae for these elements, albeit here only 80-85 % of the signal power is produced by them. Similarly to the page diagonal elements, to achieve constant elements in the $dq0$ system, we set the amplitudes of the first spatial harmonics to $\Gamma_0/\sqrt{3}$.

These six measured curves determine twelve elements, due to the symmetries of the Hessian matrices. The idealized formulae are (61)–(66).

$$\Gamma_{aab}(\vartheta) = \Gamma_{aba}(\vartheta) = -\frac{\Gamma_0}{\sqrt{3}}\cos(\vartheta - 150^\circ) \quad (61)$$

$$\Gamma_{bbc}(\vartheta) = \Gamma_{bcb}(\vartheta) = -\frac{\Gamma_0}{\sqrt{3}}\cos(\vartheta + 90^\circ) \quad (62)$$

$$\Gamma_{cca}(\vartheta) = \Gamma_{cac}(\vartheta) = -\frac{\Gamma_0}{\sqrt{3}}\cos(\vartheta - 30^\circ) \quad (63)$$

$$\Gamma_{bba}(\vartheta) = \Gamma_{bab}(\vartheta) = -\frac{\Gamma_0}{\sqrt{3}}\cos(\vartheta + 30^\circ) \quad (64)$$

$$\Gamma_{ccb}(\vartheta) = \Gamma_{cbc}(\vartheta) = -\frac{\Gamma_0}{\sqrt{3}}\cos(\vartheta - 90^\circ) \quad (65)$$

$$\Gamma_{aac}(\vartheta) = \Gamma_{aca}(\vartheta) = -\frac{\Gamma_0}{\sqrt{3}}\cos(\vartheta + 150^\circ) \quad (66)$$

Fig. 20 shows the curves of the remaining elements that have three different indices. These determine six elements of the Hessian matrix due to its symmetries. To achieve constant elements in $dq0$, these must be equal to 0 H/A.

Since the values of these elements are smaller than the previous elements of the Hessian and they have no clear rotor-position dependence, we assigned a constant 0 H/A value to them.

$$\Gamma_{cab} = \Gamma_{abc} = \Gamma_{bca} = \Gamma_{cba} = \Gamma_{acb} = \Gamma_{bac} = 0\,\frac{\text{H}}{\text{A}} \quad (67)$$

The polarity-dependent saliency coefficient Γ_0 value that yields the best fit to the main diagonal elements is

$$\Gamma_0 = 0.162\,\frac{\mu\text{H}}{\text{A}}. \quad (68)$$

The ratio of the amplitudes of the idealized formulae of the main diagonal elements to the other elements was $\sqrt{3} \approx 1.732$, while the average ratio based on the measurement data was 1.986, which we considered acceptable.

It is important to note that the variation in the inductances and Hessian elements imply that the phase windings are not perfectly identical.

D. PARK TRANSFORMATION OF THE HESSIAN MATRIX

The next step for building the machine model was the Park transformation of the idealized Hessian matrix and the measured data. We developed and used (69) to compute the Park or $dq0$ transform of the flattened 9×3 Hessian matrix defined by (9). $\underline{T}(\vartheta)$ stands for the Park transformation matrix (47). $\underline{T}^T(\vartheta)$ and $\underline{T}^{-1}(\vartheta)$ represent the transpose and inverse of $\underline{T}$, respectively. $\underline{T}^{T^{-1}}(\vartheta) = (\underline{T}^T(\vartheta))^{-1}$ denotes the inverse of the transpose. The operator $\otimes$ refers to the Kronecker product.

$$\underline{\Gamma}_{dq0} = \left(\underline{I}_3 \otimes \underline{T}^{T^{-1}}(\vartheta)\right)\left(\underline{T}(\vartheta) \otimes \underline{I}_3\right)\underline{\Gamma}_{abc}(\vartheta)\,\underline{T}^{-1}(\vartheta) \quad (69)$$

We developed and used (70) to compute the inverse Park transform of the flattened Hessian matrix.

$$\underline{\Gamma}_{abc}(\vartheta) = \left(\underline{I}_3 \otimes \underline{T}^T(\vartheta)\right)\left(\underline{T}^{-1}(\vartheta) \otimes \underline{I}_3\right)\underline{\Gamma}_{dq0}\underline{T}(\vartheta) \quad (70)$$

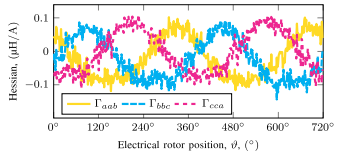

FIGURE 18. The identified non-diagonal symmetric $\Gamma_{ggp} = \Gamma_{gpg}$ elements of the Hessian calculated from 3×400 two-phase excitation measurements.

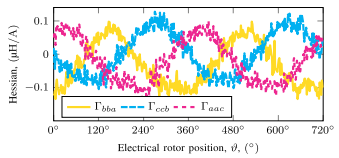

FIGURE 19. The identified non-diagonal symmetric $\Gamma_{ppg} = \Gamma_{pgp}$ elements of the Hessian calculated from 3×400 two-phase excitation measurements.

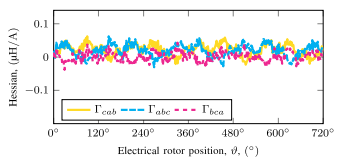

FIGURE 20. The identified non-diagonal symmetric $\Gamma_{ngp} = \Gamma_{npg}$ elements of the Hessian calculated from 3×400 two-phase excitation measurements.

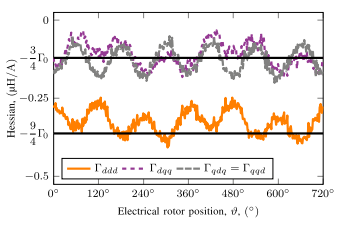

FIGURE 21. The significant elements of the $dq0$ Hessian matrix calculated from the data acquired during 3×400 single-phase and 3×400 two-phase excitation measurements and compared to the idealized model values (71).

We performed the Park transformation on the abc Hessian defined by the idealized formulae (52)–(67) and obtained the idealized $dq0$ Hessian (71).

$$\underline{\Gamma}_{dq0} = \begin{bmatrix} -\frac{9}{4}\Gamma_0 & 0 & 0 \\ 0 & -\frac{3}{4}\Gamma_0 & 0 \\ 0 & 0 & 0 \\ 0 & -\frac{3}{4}\Gamma_0 & 0 \\ -\frac{3}{4}\Gamma_0 & 0 & 0 \\ 0 & 0 & 0 \\ 0 & 0 & 0 \\ 0 & 0 & 0 \\ 0 & 0 & 0 \end{bmatrix} \quad (71)$$

Based on the properties of the inductance matrix, our hypothesis was that if we assign the correct formulae to the elements of the abc Hessian, then the elements of the $dq0$ Hessian will be constants. (71) fulfills this requirement, moreover, its elements are not only constants but similarly to the $dq0$ inductance matrix (48), many of them, for example, those that have 0 in their indices, are zero. The non-zero elements are

$$\Gamma_{ddd} = -\frac{9}{4}\Gamma_0 = -0.369\,\frac{\mu\text{H}}{\text{A}}, \text{ and} \quad (72)$$

$$\Gamma_{dqq} = \Gamma_{qdq} = \Gamma_{qqd} = -\frac{3}{4}\Gamma_0 = -0.123\,\frac{\mu\text{H}}{\text{A}}. \quad (73)$$

Fig. 21 shows the non-zero elements of the non-idealized Park-transformed Hessian using the abc measurement data shown in Figs. (15)–(20) instead of (71) and compares them to the idealized values predicted by (72) and (73). The idealized model predicts the mean values correctly but the data shows third spatial harmonics. We decided not to include these third spatial harmonics in the model to ensure that the description of the quadratic term of the flux model (10) requires only a single new machine parameter, the polarity-dependent saliency coefficient Γ_0.

VI. THE VOLTAGE EQUATION IN THE DQ0 SYSTEM

The simulation and vector control of the three-phase AC machines are usually performed in the rotor-oriented $dq0$ coordinate system or reference frame. In a star-connected machine, the zero sequence voltages, currents and flux-linkages are zero, however, the zero sequence equation was not omitted because it is necessary to the transformation of the coefficient matrices.

The Park transformed voltage, current and flux-linkage are $\underline{u}_{dq0} = \underline{T}(\vartheta)\,\underline{u}_{abc}$, $\underline{i}_{dq0} = \underline{T}(\vartheta)\,\underline{i}_{abc}$ and $\underline{\Psi}_{dq0} = \underline{T}(\vartheta)\,\underline{\Psi}_{abc}$, respectively. By using them, the abc voltage equation (2) can be transformed into the $dq0$ system (74).

$$\underline{u}_{dq0} = R\underline{i}_{dq0} + \frac{\mathrm{d}\underline{\Psi}_{dq0}}{\mathrm{d}t} + \omega\begin{bmatrix} 0 & -1 & 0 \\ 1 & 0 & 0 \\ 0 & 0 & 0 \end{bmatrix}\underline{\Psi}_{dq0} \quad (74)$$

The third term on the right-hand side of the voltage equation is the rotational voltage, which is zero at standstill because it incorporates the electrical angular velocity of the rotor, ω, as a factor.

Similarly to (10) in the abc system, we extended the $dq0$ flux-linkage vector $\underline{\Psi}_{dq0}$ with the quadratic term, using the $dq0$ Hessian defined by (69).

$$\underline{\Psi}_{dq0} = \underline{\Psi}^{PM}_{dq0} + \underline{L}_{dq0}\underline{i}_{dq0} + \frac{1}{2}\left(\underline{I}_3 \otimes \underline{i}^T_{dq0}\right)\underline{\Gamma}_{dq0}\underline{i}_{dq0} \quad (75)$$

The $\underline{\Psi}_{dq0}$ flux-linkage depends only on $\underline{i}_{dq0}$. Its coefficients are independent from the rotor position and, therefore, are constant.

For initial position detection, the voltage equation can be formulated by substituting (75) and an angular velocity of zero into (74).

$$\underline{u}_{dq0} = R\underline{i}_{dq0} + \underline{L}_{dq0}\frac{\mathrm{d}\underline{i}_{dq0}}{\mathrm{d}t} + \left(\underline{I}_3 \otimes \underline{i}^T_{dq0}\right)\underline{\Gamma}_{dq0}\frac{\mathrm{d}\underline{i}_{dq0}}{\mathrm{d}t} \quad (76)$$

The structure of (76) and (11) are very similar and their physical meaning is equivalent. Both are valid only at a standstill.

A. RELATIONSHIP TO A CURRENT-DEPENDENT INDUCTANCE MODEL

Similarly to (12), it is possible to reformulate (76) to a seemingly linear form that involves a current dependent inductance matrix.

$$\underline{u}_{dq0} = R\underline{i}_{dq0} + \underbrace{\left(\underline{L}_{dq0} + \left(\underline{I}_3 \otimes \underline{i}^T_{dq0}\right)\underline{\Gamma}_{dq0}\right)}_{\underline{L}^{\text{cdi}}_{dq0}(\underline{i}_{dq0})}\frac{\mathrm{d}\underline{i}_{dq0}}{\mathrm{d}t} \quad (77)$$

Here, $\underline{L}^{\text{cdi}}_{dq0}(\underline{i}_{dq0})$ is the current dependent $dq0$ inductance matrix which is a linear function of $\underline{i}_{dq0}$. Its constant term is the differential inductance matrix $\underline{L}_{dq0}$ and the coefficient matrix of its linear term is the Hessian $\underline{\Gamma}_{dq0}$. The current dependent elements of $\underline{L}^{\text{cdi}}_{dq0}(\underline{i}_{dq0})$ are

$$L^{\text{cdi}}_{dd}(\underline{i}_{dq0}) = L_{dd} + \Gamma_{ddd}i_d = L_{dd} - \frac{9}{4}\Gamma_0 i_d, \quad (78)$$

$$L^{\text{cdi}}_{dq}(\underline{i}_{dq0}) = \Gamma_{dqq}i_q = -\frac{3}{4}\Gamma_0 i_q, \quad (79)$$

$$L^{\text{cdi}}_{qd}(\underline{i}_{dq0}) = \Gamma_{qqd}i_q = -\frac{3}{4}\Gamma_0 i_q \quad \text{and} \quad (80)$$

$$L^{\text{cdi}}_{qq}(\underline{i}_{dq0}) = L_{qq} + \Gamma_{qdq}i_d = L_{qq} - \frac{3}{4}\Gamma_0 i_d. \quad (81)$$

Equations (78)–(80) are linear models for main flux saturation and cross-saturation [17]. Γ_0 is a positive constant. Therefore, our model predicts that positive i_d decreases the current-dependent self-inductances while positive i_q decreases the current-dependent mutual inductances. Γ_0 is not specific to either d direction or q direction and is not specific to the main flux saturation or cross-saturation but is a coefficient that globally describes the susceptibility of the machine to polarity-dependent saturation.

VII. MACHINE-MODEL VALIDATION

We analyzed the transient behavior as well as the rotor-position dependency of our machine model and compared it to the measurements. Based on (76), the d and q direction voltage equations are (82) and (83), respectively.

$$u_d = Ri_d + L_{dd}\frac{\mathrm{d}i_d}{\mathrm{d}t} + \frac{1}{2}\Gamma_{ddd}\frac{\mathrm{d}i_d^2}{\mathrm{d}t} + \frac{1}{2}\Gamma_{dqq}\frac{\mathrm{d}i_q^2}{\mathrm{d}t} \quad (82)$$

$$u_q = Ri_q + L_{qq}\frac{\mathrm{d}i_q}{\mathrm{d}t} + \Gamma_{qdq}\frac{\mathrm{d}i_di_q}{\mathrm{d}t} \quad (83)$$

Unlike in the linear machine model, both dq voltage equations contain both dq currents. In our numerical simulation-based analysis, we used the separated forms (84) and (85).

$$\frac{\mathrm{d}i_d}{\mathrm{d}t} = \frac{(L_{qq}+\Gamma_{qdq}i_d)(u_d-Ri_d)-\Gamma_{dqq}i_q(u_q-Ri_q)}{(L_{dd}+\Gamma_{ddd}i_d)(L_{qq}+\Gamma_{qdq}i_d)-\Gamma_{dqq}\Gamma_{qdq}i_q^2} \quad (84)$$

$$\frac{\mathrm{d}i_q}{\mathrm{d}t} = \frac{(L_{dd}+\Gamma_{ddd}i_d)(u_q-Ri_q)-\Gamma_{qdq}i_q(u_d-Ri_d)}{(L_{dd}+\Gamma_{ddd}i_d)(L_{qq}+\Gamma_{qdq}i_d)-\Gamma_{dqq}\Gamma_{qdq}i_q^2} \quad (85)$$

The divisions limit the domain of the differential equation system. In the case of our test motors, the absolute value of i_q must be smaller than $1349.5\,\mathrm{A}$ to avoid division by zero, which is much higher than the physically realizable current and, therefore, does not provide a practical limitation.

The electromagnetic torque, M_E, calculated as the derivative of the magnetic coenergy, is equal to

$$\frac{3}{2}z_P\left(\Psi_{PM}i_q - (L_{qq}-L_{dd})i_di_q - \frac{3}{8}\Gamma_0 i_q(i_d^2+i_q^2)\right). \quad (86)$$

The third term introduced by the quadratic term of the flux-linkage is very small; at the starting current, it is about $0.7\,\%$ of the torque of the permanent magnets.

A. THEORETICAL TRANSIENT BEHAVIOR

We started the analysis of the transient behavior by determining the analytical solution for step voltage injection in the d direction. In this case, only d direction voltage and current are present, and (82) can be simplified to

$$u_d = Ri_d + (L_{dd}+\Gamma_{ddd}i_d)\frac{\mathrm{d}i_d}{\mathrm{d}t}, \quad (87)$$

which is a special case of the Abel differential equation of the second kind. The analytical solution for $u_d = U_0 1(t)$ where $1(t)$ denotes the Heaviside step function and the initial condition $i_d(0\,\mathrm{s}) = 0\,\mathrm{A}$ is

$$i_d(t) = \frac{U_0}{R} + \frac{L_{dd}R + U_0\Gamma_{ddd}}{R\Gamma_{ddd}}W_0\big(y(t)\big) \quad (88)$$

where W_0 represents the principal branch of the Lambert W function, also referred to as the product logarithm function [49]. The inner function is

$$y(t) = -\frac{U_0\Gamma_{ddd}}{L_{dd}R + U_0\Gamma_{ddd}}\exp\left(-\frac{R^2t + U_0\Gamma_{ddd}}{L_{dd}R + U_0\Gamma_{ddd}}\right). \quad (89)$$

We calculated the theoretical phase current responses in phase a using (88) and (89) for both positive and negative step-voltage injections in the direction of the phase itself at both poles, then compared them to the linear solution

$$i_a^{\mathrm{lin}} = \frac{U_0}{R}\left(1 - \mathrm{e}^{-\frac{R}{L_{dd}}t}\right) \quad (90)$$

and each other. The current responses are plotted in Fig. 22 using $5\Gamma_{ddd}$ to emphasize the otherwise very small effect of the quadratic term. The amplitude of the steps was $U_0 = 24\,\mathrm{V}$ which corresponds to a DC-link voltage of $U_{DC} = 36\,\mathrm{V}$. The stationary solutions of the linear as well as nonlinear models are equal in each case and their absolute value is U_0/R.

The transients of the linear and nonlinear models are different, moreover, the sign of the current difference $\Delta i = i_a - i_a^{\mathrm{lin}}$ in the transient intervals depends on the magnet polarity. At the north pole, the positive current response rises faster than the linear solution, while the negative response rises more slowly and $\Delta i \geq 0\,\mathrm{A}$. At the south pole, the opposite occurs, that is the negative current response rises faster and $\Delta i \leq 0\,\mathrm{A}$. Although this behavior is somewhat similar to linear systems that have different time constants or different inductances, it is actually a nonlinearity.

In the early stage of the injection, the current rises almost linearly, but due to the quadratic nature of the nonlinearity, the difference between the linear and nonlinear solutions rises very slowly. Moreover, when the difference becomes sufficiently large to measure, the current is already very high. Furthermore, polarity detection by comparing a single pulse to the linear solution would require a very precise linear model. Both problems can be mitigated by comparing the current responses of the positive and negative pulses as well as performing measurements on all three phases.

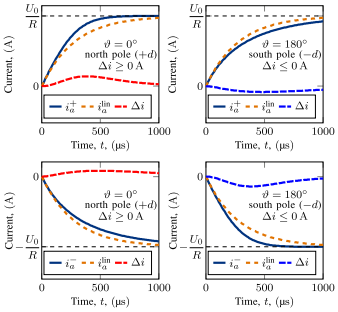

FIGURE 22. The magnet polarity-dependent effect of the nonlinearity on the phase current response to positive and negative voltage steps in the $+d$ and $-d$ directions, calculated using $5\Gamma_{ddd}$ from (72) to emphasize the otherwise very small effect of the quadratic term.

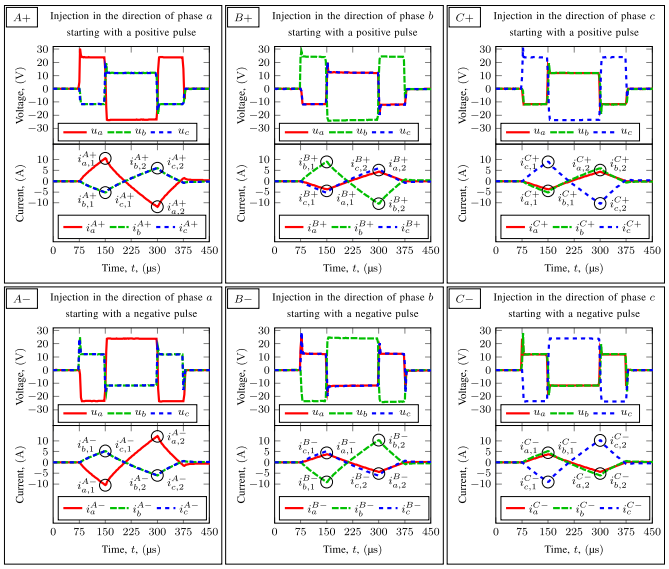

FIGURE 23. Measurements of the current responses to the three-phase voltage injection steps at a fixed rotor position.

B. THREE-PHASE EXCITATION MEASUREMENTS

We performed measurements using the three-phase injection scheme shown in Fig. 23 to collect data for the validation of the extended machine model proposed in the previous sections and to develop an initial position detection method that is capable of polarity detection. A single injection step starts with a $75\,\mu\mathrm{s}$-long continuous, non-modulated voltage pulse in the reference direction. This is followed by a $150\,\mu\mathrm{s}$-long voltage pulse in the opposite direction and the third voltage pulse is $75\,\mu\mathrm{s}$-long in the reference direction again. We used this single period even square wave voltage signal because it has a current response that is close to symmetric and the change in the angular momentum of the rotor is negligible compared to an odd square wave.

The voltage injection scheme performed at a given rotor position involves all six possible steps for three phases (A, B, C) as well as a positive and negative starting pulse ($+/-$). The corresponding switching sequences are listed in Table 5. The six steps were repeated at all 400 rotor positions resulting in 2400 measurements. We measured the currents with a sample time of $T_S = 2.5\,\mu\mathrm{s}$ to validate the model. Although the sampling time of the voltages was $75\,\mathrm{ns}$ to more accurately capture the switching transients, we downsampled them to match the sampling time of the current data. We used the star point to measure the phase voltages, but the current remained negligible using a $1\,\mathrm{M}\Omega$ oscilloscope input.

TABLE 5. The switching sequences of the steps of the three-phase voltage injection scheme.

Step	Switching sequence				
	idle	75 µs	150 µs	75 µs	fade-out
$A+$	(000)	(100)	(011)	(100)	(000)
$A-$	(000)	(011)	(100)	(011)	(000)
$B+$	(000)	(010)	(101)	(010)	(000)
$B-$	(000)	(101)	(010)	(101)	(000)
$C+$	(000)	(001)	(110)	(001)	(000)
$C-$	(000)	(110)	(001)	(110)	(000)

C. COMPARISON OF MEASURED AND SIMULATED TRANSIENT BEHAVIOR

The nonlinear machine model predicts that the Δi deviations from the linear model at a certain rotor position have the same sign for a positive and a negative step (see Fig. 22). To amplify the effect of the polarity-dependent nonlinearity, we calculated the Δi_a^A phase current difference as the sum of the $A+$ and $A-$ current responses.

$$\Delta i_a^A = i_a^{A+} + i_a^{A-} \quad (91)$$

The current responses of the injected single period even square wave voltage signals rise in the reference direction, then in the opposite direction, producing effectively two step responses with opposite signs (see Fig. 23). The sign of the phase current difference Δi_a^A is determined by the magnet polarity (positive at the north pole and negative at the south pole). The waveform of Δi_a^A is shaped by the quadratic nonlinearity. As the current rises and falls almost linearly, Δi_a^A has sections that resemble to parabolae.

Figs. 24 and 25 show the measured and simulated phase current differences for phase a at 0° (north pole) and 180° (south pole), respectively. We calculated $\Delta i_a^{A\mathrm{sim}}$ by a numerical simulation based on (84) and (85). Our extended machine model correctly predicts the waveform of the phase current difference, moreover, the peak values at $150\,\mu\mathrm{s}$ and $300\,\mu\mathrm{s}$ are sufficiently accurate.

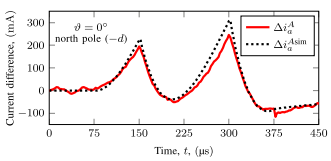

FIGURE 24. Comparison of measured and simulated phase current differences at $\vartheta = 0°$ (north pole).

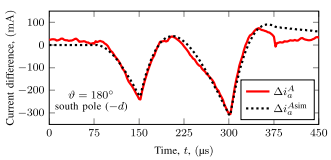

FIGURE 25. Comparison of measured and simulated phase current differences at $\vartheta = 180°$ (south pole).

D. COMPARISON OF MEASURED AND SIMULATED ROTOR-POSITION DEPENDENCY

The six injection steps shown in Fig. 23 produce 18 peak phase current values for the first peak ($k=1$, $t = 150\,\mu\mathrm{s}$) and another 18 values for the second peak ($k = 2$, $t = 300\,\mu\mathrm{s}$). Since all these current values hold information about the rotor position and polarity, we developed a method that combines all of them. In the first step, we rearranged the peak values of the phase current responses into mean and difference values as stated in (92)-(94) using the generalized indexing presented in Table 3.

$$i_{g,k}^G = \frac{1}{2}\left(i_{g,k}^{G+} - i_{g,k}^{G-}\right), \quad \Delta i_{g,k}^G = i_{g,k}^{G+} + i_{g,k}^{G-} \quad (92)$$

$$i_{p,k}^G = \frac{1}{2}\left(i_{p,k}^{G+} - i_{p,k}^{G-}\right), \quad \Delta i_{p,k}^G = i_{p,k}^{G+} + i_{p,k}^{G-} \quad (93)$$

$$i_{n,k}^G = \frac{1}{2}\left(i_{n,k}^{G+} - i_{n,k}^{G-}\right), \quad \Delta i_{n,k}^G = i_{n,k}^{G+} + i_{n,k}^{G-} \quad (94)$$

Given that the rotor-position dependency of the mean current values is mainly influenced by the inductances, they have significant second spatial harmonics, while the phase current differences are a consequence of the quadratic nonlinearity characterized by the elements of the Hessian matrix and have dominant first spatial harmonics. Figs. 26–28 show the measured and simulated values for the phase current differences $\Delta i_{g,1}^G$, $\Delta i_{p,1}^G$ and $\Delta i_{n,1}^G$.

The phase current difference curves are shifted by 120°, as expected for a three-phase machine. The measurements confirm the presence of a dominant first spatial harmonic but also show third spatial harmonics that render the phase current difference curves triangular, especially for the Δi_g^G curves. The simulated curves show that our extended machine model correctly captures these characteristics of the machine as well as predicts the spatial distribution and values of the phase current differences with a sufficient degree of accuracy to be used in the design of a polarity detection method. One small but systematic difference between the measured and simulated values can be seen; the measured values are spatially shifted by several electrical degrees.

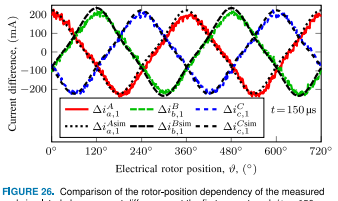

FIGURE 26. Comparison of the rotor-position dependency of the measured and simulated phase current differences at the first current peak ($t = 150\,\mu\mathrm{s}$, 3×400 measurement points, 3×400 simulation points).

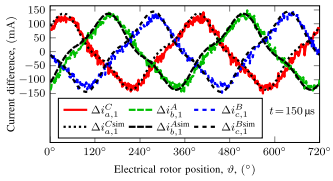

FIGURE 27. Comparison of the rotor-position dependency of the measured and simulated phase current differences at the first current peak ($t = 150\,\mu\mathrm{s}$, 3×400 measurement points, 3×400 simulation points).

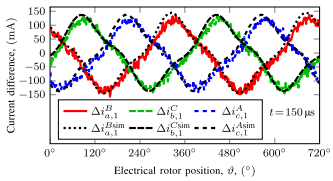

FIGURE 28. Comparison of the rotor position dependency of the measured and simulated phase current differences at the first current peak ($t = 150\,\mu\mathrm{s}$, 3×400 measurement points, 3×400 simulation points).

VIII. INITIAL POSITION DETECTION METHOD

Our initial position detection method uses either the first or second peak current values sampled at $150\,\mu\mathrm{s}$ ($k = 1$) and $300\,\mu\mathrm{s}$ ($k = 2$), respectively, as shown in Fig. 23. We rearranged the 18 peak phase current values produced by the six injection steps into mean and difference values as stated in (92)–(94) to separate the significant even and odd spatial harmonics. This produces 9 mean values and 9 difference values for a single k index. Our method then combines them into 3 mean and 3 difference values to retain all the rotor position-dependent harmonic content while lowering the number of variables to be processed and increasing the signal-to-noise ratio.

We calculated the combined mean and difference values for index k using (95)–(97).

$$i_k^A = i_{a,k}^A + i_{b,k}^C + i_{c,k}^B, \quad \Delta i_k^A = \Delta i_{a,k}^A - \Delta i_{b,k}^A - \Delta i_{c,k}^A \quad (95)$$

$$i_k^B = i_{b,k}^B + i_{c,k}^A + i_{a,k}^C, \quad \Delta i_k^B = \Delta i_{b,k}^B - \Delta i_{c,k}^B - \Delta i_{a,k}^B \quad (96)$$

$$i_k^C = i_{c,k}^C + i_{b,k}^A + i_{a,k}^B, \quad \Delta i_k^C = \Delta i_{c,k}^C - \Delta i_{a,k}^C - \Delta i_{b,k}^C \quad (97)$$

Figs. 29 and 30 show the rotor-position dependency of the combined mean values. The combined mean value curves have a dominant second spatial harmonic, moreover, as a result of the combination of positive and negative phase currents, their offset value is zero. Their amplitude is somewhat larger at the second peak, and they have opposite sign there.

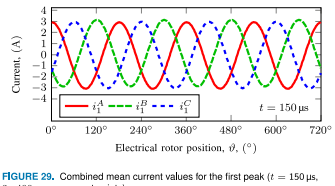

FIGURE 29. Combined mean current values for the first peak ($t = 150\,\mu\mathrm{s}$, 3×400 measurement points).

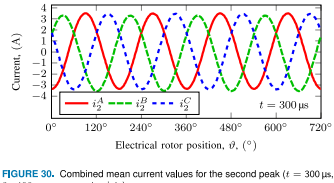

FIGURE 30. Combined mean current values for the second peak ($t = 300\,\mu\mathrm{s}$, 3×400 measurement points).

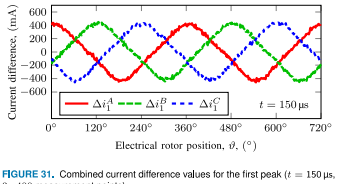

FIGURE 31. Combined current difference values for the first peak ($t = 150\,\mu\mathrm{s}$, 3×400 measurement points).

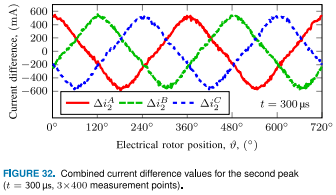

FIGURE 32. Combined current difference values for the second peak ($t = 300\,\mu\mathrm{s}$, 3×400 measurement points).

Figs. 31 and 32 show the rotor-position dependency of the combined differences that have a dominant first spatial harmonic as well as inherit the slightly triangular shape and zero offset from the phase current differences. Similarly to

the combined mean currents, slightly larger amplitudes can be seen at the second peak.

A. ROTOR-POSITION CALCULATION BASED ON THE COMBINED MEAN CURRENTS

We calculated the rotor position based on the combined mean current values or the combined current difference values for both peaks (95)–(97). In both cases, three spatially shifted sinusoidal curves with equal amplitudes and zero offsets are observed. In the following sections, we present methods to calculate the rotor position based on them.

Let A_1 denote the amplitude of the combined mean currents at the first peak (see Fig. 29), $\alpha_1^M = A_1\cos(2\vartheta)$ and $\beta_1^M = A_1\sin(2\vartheta)$. The combined mean currents are formulated as cosines shifted by multiples of 120° and use the trigonometric addition formulae used to decompose them into linear combinations of α_1^M and β_1^M. The resulting equation system (98) is overdetermined.

$$\begin{bmatrix} i_1^A \\ i_1^B \\ i_1^C \end{bmatrix} = \begin{bmatrix} A_1\cos(2\vartheta) \\ A_1\cos(2\vartheta+120°) \\ A_1\cos(2\vartheta+240°) \end{bmatrix} = \begin{bmatrix} 1 & 0 \\ -\frac{1}{2} & -\frac{\sqrt{3}}{2} \\ -\frac{1}{2} & \frac{\sqrt{3}}{2} \end{bmatrix} \begin{bmatrix} \alpha_1^M \\ \beta_1^M \end{bmatrix} \tag{98}$$

The solutions of the equation system obtained by the method of ordinary least squares are

$$\alpha_1^M = \frac{2}{3}i_1^A - \frac{1}{3}i_1^B - \frac{1}{3}i_1^C, \quad \beta_1^M = -\frac{i_1^B}{\sqrt{3}} + \frac{i_1^C}{\sqrt{3}}. \tag{99}$$

The coefficient matrix on the right-hand side of (98) is similar to the Clarke transform matrix, moreover, α_1^M and β_1^M can be interpreted as two-phase coordinates of the combined mean current vector that points in the direction of 2ϑ.

For the second peak, we have to modify the equation system because the combined mean current curves have the opposite sign here (see Fig. 30).

$$\begin{bmatrix} i_2^A \\ i_2^B \\ i_2^C \end{bmatrix} = \begin{bmatrix} -A_2\cos(2\vartheta) \\ -A_2\cos(2\vartheta+120°) \\ -A_2\cos(2\vartheta+240°) \end{bmatrix} = \begin{bmatrix} -1 & 0 \\ \frac{1}{2} & \frac{\sqrt{3}}{2} \\ \frac{1}{2} & -\frac{\sqrt{3}}{2} \end{bmatrix} \begin{bmatrix} \alpha_2^M \\ \beta_2^M \end{bmatrix} \tag{100}$$

The solutions of the equation system in this case are

$$\alpha_2^M = -\frac{2}{3}i_2^A + \frac{1}{3}i_2^B + \frac{1}{3}i_2^C, \quad \beta_2^M = \frac{i_2^B}{\sqrt{3}} - \frac{i_2^C}{\sqrt{3}}. \tag{101}$$

The mean-current-based rotor-position estimation $\hat{\vartheta}_k^M$ can be calculated for both peaks using the 2-argument arctangent function $\operatorname{atan2}(y,x)$.

$$\hat{\vartheta}_k^M = \frac{1}{2}\operatorname{atan2}\left(\beta_k^M, \alpha_k^M\right) \tag{102}$$

Fig. 33 shows the estimated rotor positions. Both $\hat{\vartheta}_1^M$ and $\hat{\vartheta}_2^M$ have an ambiguity of 180°. Their value is confined to the $[-90°, 90°]$ interval.

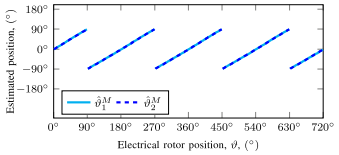

FIGURE 33. The estimated rotor position based on the combined mean currents (2×400 measurement points).

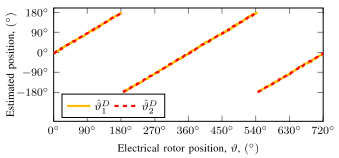

FIGURE 34. The estimated rotor position based on the combined current differences (2×400 measurement points).

B. ROTOR-POSITION CALCULATION BASED ON THE COMBINED CURRENT DIFFERENCES

Let A_k denote the amplitude of the combined current differences at peak k (see Figs. 31 and 32). These curves have dominant first spatial harmonics, so let $\alpha_k^D = A_k\cos(\vartheta)$ and $\beta_k^D = A_k\sin(\vartheta)$. The combined current differences are formulated as cosines shifted by multiples of 120° and the trigonometric addition formulae used to decompose them into linear combinations of α_k^D and β_k^D.

$$\begin{bmatrix} \Delta i_k^A \\ \Delta i_k^B \\ \Delta i_k^C \end{bmatrix} = \begin{bmatrix} A_k\cos(\vartheta) \\ A_k\cos(\vartheta-120°) \\ A_k\cos(\vartheta-240°) \end{bmatrix} = \begin{bmatrix} 1 & 0 \\ -\frac{1}{2} & \frac{\sqrt{3}}{2} \\ -\frac{1}{2} & -\frac{\sqrt{3}}{2} \end{bmatrix} \begin{bmatrix} \alpha_k^D \\ \beta_k^D \end{bmatrix} \tag{103}$$

The solutions of the equation system for the two-phase coordinates are

$$\alpha_k^D = \frac{2}{3}\Delta i_k^A - \frac{1}{3}\Delta i_k^B - \frac{1}{3}\Delta i_k^C, \quad \beta_k^D = \frac{\Delta i^B}{\sqrt{3}} - \frac{\Delta i^C}{\sqrt{3}}. \tag{104}$$

To calculate the current-difference-based estimate of the rotor position $\hat{\vartheta}_k^D$, once again the 2-argument arctangent function $\operatorname{atan2}(y,x)$ was used.

$$\hat{\vartheta}_k^D = \operatorname{atan2}\left(\beta_k^D, \alpha_k^D\right) \tag{105}$$

Fig. 34 shows the estimated rotor positions. $\hat{\vartheta}_1^D$ and $\hat{\vartheta}_2^D$ have no ambiguity. They cover the entirety of the $[-180°, 180°]$ interval.

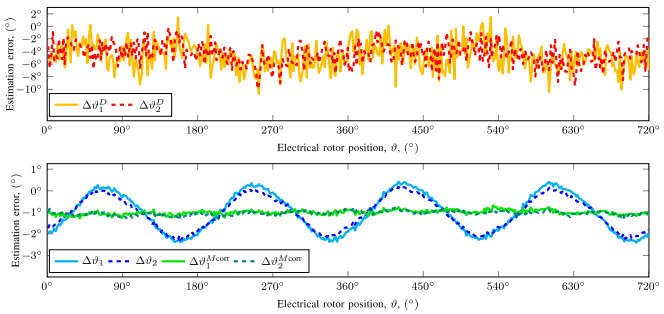

FIGURE 35. The errors of the mean-current-based and current-difference-based rotor position estimates ((2+4)×400 measurement points).

C. ESTIMATION-ERROR EVALUATION

The unbounded domain of the rotor position and the bounded domains of the estimated values have to be taken into account when computing the estimation errors. The error of the current-difference-based rotor-position estimate is therefore

$$\Delta\vartheta_k^D = \hat{\vartheta}_k^D - \operatorname{mod}(\vartheta+180°, 360°) + 180°. \tag{106}$$

The $\Delta\vartheta_k^D$ estimation errors are plotted in Fig. 35. The estimation errors at both peaks are offset, by −4.66° at the first and −4.37° at the second peak. The standard deviations are 2.13° and 1.68°, respectively.

The mean-current-based estimates of the rotor position have to be corrected based on the difference-based estimate to eliminate the ±180° ambiguity.

$$\hat{\vartheta}_k = \begin{cases} \hat{\vartheta}_k^M + 180° & \hat{\vartheta}_k^D - \hat{\vartheta}_k^M > 90°, \\ \hat{\vartheta}_k^M & 90° \geq \hat{\vartheta}_k^D - \hat{\vartheta}_k^M \geq -90°, \\ \hat{\vartheta}_k^M - 180° & -90° > \hat{\vartheta}_k^D - \hat{\vartheta}_k^M. \end{cases} \tag{107}$$

Equation (107) corrects the estimates in the $[-180°, 180°]$ interval. Depending on the interval used to represent angles, other correction methods may be necessary.

The error of the polarity-corrected mean-current-based rotor-position estimate is

$$\Delta\vartheta_k = \hat{\vartheta}_k - \operatorname{mod}(\vartheta+180°, 360°) + 180°. \tag{108}$$

The $\Delta\vartheta_k$ estimation errors are plotted in Fig. 35. The estimation errors at both peaks are offset, by −1.01° at the first and −1.04° at the second peak.

D. WINDING DIFFERENCE CORRECTION

Unlike the error of the difference-based estimate, $\Delta\vartheta_k$ has a clear second spatial harmonic at both peaks. We attributed this to the small differences of the phase windings and developed a correction method. We modified (98) and (100) to take into account the difference between the amplitudes of the i_k^G curves (A_k^G) and their offsets (B_k^G). Table 6 lists the parameters fitted to the combined mean current curves shown in Figs. 29 and 30.

TABLE 6. The fitted parameters of the combined mean current curves.

Amplitudes		
$A_1^A = 3.0047$ A	$A_1^B = 3.0042$ A	$A_1^C = 3.0057$ A
$A_2^A = 3.4133$ A	$A_2^B = 3.4136$ A	$A_2^C = 3.416$ A
Offsets		
$B_1^A = -81.2$ mA	$B_1^B = 130.3$ mA	$B_1^C = -37.5$ mA
$B_2^A = 81.2$ mA	$B_2^B = -123.2$ mA	$B_2^C = 30.7$ mA

We replaced the combined means current with their offset-free and normalized values, $i_k^{G\text{corr}}$, in (99) and (101).

$$i_k^{G\text{corr}} = \frac{i_k^G - B_k^G}{A_k^G} \tag{109}$$

Let the corrected two-phase coordinates be $\alpha_k^{M\text{corr}}$ and $\beta_k^{M\text{corr}}$. The corrected estimate is

$$\hat{\vartheta}_k^{M\text{corr}} = \frac{1}{2}\operatorname{atan2}\left(\beta_k^{M\text{corr}}, \alpha_k^{M\text{corr}}\right). \tag{110}$$

Equation (107) has to be applied. The errors of the corrected estimates denoted by $\Delta\vartheta_k^{M\text{corr}}$ are plotted in Fig. 35. Although the correction eliminates the second spatial harmonic at both peaks, the offsets are unaffected.

The error of the current-difference-based estimate is much larger and noisier than the error of the mean-current-based estimate. Therefore, we only used the $\hat{\vartheta}_k^D$ values to eliminate the polarity error of $\hat{\vartheta}_k^M$ and $\hat{\vartheta}_k^{M\text{corr}}$.

E. THE ESTIMATION-ERROR OFFSETS AND THE TRUE ROTOR POSITION

Whilst setting up and calibrating our measurement system, we determined the zero rotor position based on the torque of the machine. We excited the machine in three-phase connection with the inverter in the direction of all the phases using small positive and negative voltages for several seconds and recorded the stationary rotor positions. We performed this stepping process in both positive and negative rotational directions to eliminate frictional hysteresis. We defined the electrical rotor position ϑ used in the previous sections as the best linear fit to the torque-determined phase axes.

We can interpret the offsets of the estimates as different zero rotor positions based on the inductances or the Hessian instead of the torque. Unfortunately, these rotor position references seem to be independent and we see only measurements similar to ours as ways to determine them.

Besides the presented measurements, we also performed an other one in which the rotor from 0° to 360° was stepped and then stepped backwards back to 0° to see if a spatial lag existed between the rotor and the magnetic field in the stator core due to magnetic hysteresis. This measurement showed a very small difference (around 0.001° at both peaks) between the forward and backward rotating sections supporting the assumption that the effect of magnetic hysteresis is negligible.

IX. INITIAL POSITION DETECTION DESIGN

The performance of the proposed position and polarity detection method can be characterized by the standard deviation of the corrected rotor-position estimate and the probability of the correct polarity detection. In a given drive, these are significantly influenced by the DC-link voltage (U_{DC}), the noise of the current measurement system and, most importantly, the length of the injected even square wave. The critical decision in the design is the selection of the injection length. A longer injection results in higher currents but increases the chance of the rotor moving. A shorter injection produces smaller currents, decreasing the signal-to-noise ratio. We analyzed the performance impact of the injection length at selected DC-link voltage values and provide approximate formulae that help to determine the minimal value needed for reliable position and polarity detection when the standard deviation of the current measurement noise (σ_{CM}) is known.

The DC-link voltage depends on the supply that feeds the inverter. Its value is typically a multiple of 6 V. We repeated the three-phase measurements at 18 V, 24 V and 36 V to analyze its effect. The noise properties are hardware-dependent and cannot be changed without a redesign. Based on the current samples recorded in the idle sections before every injection, the standard deviation of the current measurement was $\sigma_{CM} = 4.4$ mA for each U_{DC} values.

A. MEAN AND DIFFERENCE APPROXIMATIONS

Fig. 36 shows the mean phase current i_a^A calculated not only for the first peak but for all samples between 75 µs and 150 µs as well as for all rotor positions. The figure also illustrates

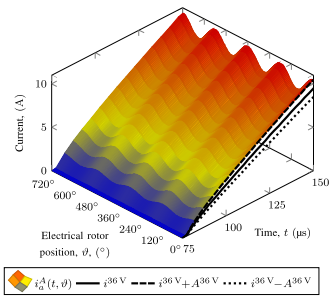

FIGURE 36. The measured mean phase current i_a^A as a function of time and rotor position.

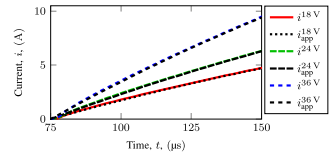

FIGURE 37. The time-dependent mean values of the mean currents and their approximations.

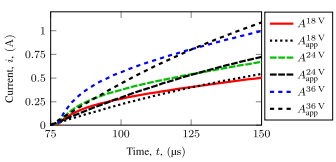

FIGURE 38. The time-dependent amplitudes of the mean currents and their approximations.

the time-dependent mean $i^{36\,\text{V}}$ and amplitude $A^{36\,\text{V}}$ that are calculated with respect to the rotor position. Their values and approximations given by (111) and (112) are plotted in Figs. 37 and 38, respectively.

$$i_{\text{app}}^{U_{DC}} \approx \frac{2}{3}\frac{U_{DC}}{R}\left(1 - \mathrm{e}^{-\frac{2R}{L_{dd}+L_{qq}}t}\right) \tag{111}$$

$$A_{\text{app}}^{U_{DC}} \approx \frac{1}{3}\frac{U_{DC}}{R}\left(\mathrm{e}^{-\frac{R}{L_{qq}}t} - \mathrm{e}^{-\frac{R}{L_{dd}}t}\right) \tag{112}$$

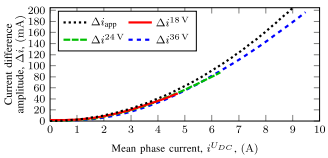

FIGURE 39. The relationship between the mean phase current and the amplitude of the phase current difference measured at several DC-link voltages and compared to the approximated value (113).

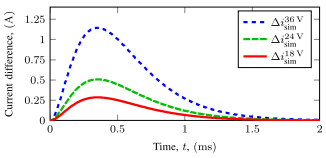

FIGURE 40. The amplitude of the phase current differences simulated for longer injections at several DC-link voltages.

Eq. (111) uses the average of L_{dd} and L_{qq} to approximate $i^{U_{DC}}$. Eq. (112) is half of the difference between the current responses in the q and d directions and is a less accurate approximation of $A^{36\,\text{V}}$. This inaccuracy can be attributed to the frequency dependence of the inductances, another type of non-linearity present in PMSMs. The high-frequency inductances tend to be lower, therefore, the currents increase faster at first than the exponential approximation and later slow down (see Fig. 38).

The detection of the polarity depends on the phase current differences defined by (92). Their amplitudes ($\Delta i^{U_{DC}}$) can be approximated as

$$\Delta i_{\text{app}} \approx -\frac{\Gamma_{ddd}}{L_{dd}}\left(i_{\text{app}}^{U_{DC}}\right)^2. \tag{113}$$

Fig. 39 shows the measured amplitudes of the phase current differences and Δi_{app} as functions of the mean phase current. The relationship is quadratic and its approximate form slightly overestimates the amplitude.

Fig. 40 shows the amplitude of the phase current differences simulated for longer injections. The amplitude has a maximum value of between one and two d direction electrical time constants. Increasing the pulse length and the currents improves the polarity detection up to this point.

B. ESTIMATION-ERROR METRICS

We applied our method to any of the 31 sampling times in the [75 µs, 150 µs] interval. In this interval, the currents behave similarly to the first peak and the corresponding formulae (99) have to be applied. Fig. 41 shows the standard deviations

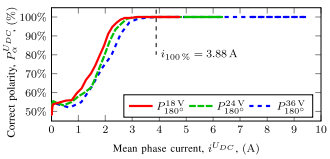

FIGURE 41. The relationship between the mean phase current and the standard deviation of the error of the corrected rotor position estimate at several DC-link voltages.

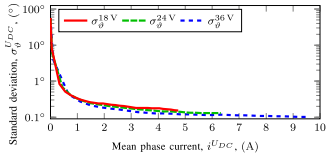

FIGURE 42. The relationship between the mean phase current and the probability of correct polarity detection at several DC-link voltages.

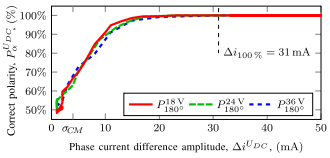

FIGURE 43. The relationship between the amplitudes of the phase current differences and the probability of correct polarity detection.

of the corrected rotor-position estimates at different DC-link voltages as functions of the mean phase current. At small currents, the estimation quickly improves as we inject longer pulses. At approximately 1 A, the improvement slows down and the current as well as the pulse length have to be increased significantly to further reduce the standard deviation of the estimation error.

The polarity is correctly detected if the absolute value of the estimation error $\Delta\vartheta^D$ of the difference-based estimate is smaller than $\alpha = 180°$. Let N_C denote the number of rotor positions where the polarity is correctly detected. Then we can define the probability of correct polarity detection ($P_\alpha^{U_{DC}}$) as the ratio of N_C to the total number of rotor positions which was 400.

$$P_\alpha^{U_{DC}} = P\left(|\Delta\vartheta^D| < \alpha\right) = \frac{N_C}{400} \tag{114}$$

The probabilities of correct polarity detection are plotted in Figs. 42 and 43 as functions of the mean phase current and the amplitude of the phase current difference, respectively. The probability of correctly detecting the position increases as the mean phase current and the amplitude of the current difference increases, however, in terms of polarity detection, only a correctness of $100\,\%$ is acceptable. The lower limits of $100\,\%$ correctness are $i_{100\,\%} = 3.88\,\mathrm{A}$ and $\Delta i_{100\,\%} = 31\,\mathrm{mA}$. By using (113) and substituting $i_{100\,\%}$, the approximated amplitude of the phase current difference is $38\,\mathrm{mA}$.

C. PULSE-LENGTH SELECTION

The measurement data show that a sufficiently high amplitude of phase current difference ensures that the polarity detection is $100\,\%$ correct. We decided to set the limitation $\Delta i_{\mathrm{design}} \geq 10\sigma_{CM}$. In our drive system, the required minimum value for the difference amplitude was

$$\Delta i_{\mathrm{design}} = 10\sigma_{CM} = 44\,\mathrm{mA}. \tag{115}$$

This value does not depend on the DC-link voltage. Using (113), the required minimum mean phase current was

$$i_{\mathrm{design}} = \sqrt{-\frac{L_{dd}}{\Gamma_{ddd}}\Delta i_{\mathrm{design}}} = 4.17\,\mathrm{A}. \tag{116}$$

The required amplitude of current difference and mean current are independent of the DC-link voltage.

By inverting (111), substituting i_{design} and solving for the time, the minimum pulse length required to fulfill (115) is obtained.

$$T_{\mathrm{design}}^{U_{DC}} = -\frac{L_{dd}+L_{qq}}{2R}\ln\left(1-\frac{3}{2}\frac{R}{U_{DC}}i_{\mathrm{design}}\right) \tag{117}$$

Table 7 lists the calculated pulse lengths.

TABLE 7. The calculated pulse lengths at several DC-link voltages.

DC-link voltage	Pulse length
U_{DC}	$T_{\mathrm{design}}^{U_{DC}}$
18 V	65.3 µs
24 V	47.4 µs
36 V	30.6 µs

A lower DC-link voltage requires a longer pulse length to achieve the desired current level. A longer pulse length has a lower fundamental harmonic and results in a higher chance or amplitude of rotor movement. During our measurements, we monitored the rotor position using the factory-mounted 13-bit encoders on the test motors. The movement of the rotor did not cross more than one bit boundary, resulting in a maximum rotor oscillation of $0.0879°$.

Since the fade-out times of the phase currents after the injections were around one millisecond long, we set the idle time between the pulses at $2\,\mathrm{ms}$. The total duration of the six injections was between 12 and $12.5\,\mathrm{ms}$. If the total duration of the initial position detection method is of concern, then the length of the second pulse in the reference direction can be shortened to stop the injection closer to the zero-crossings of the phase currents.

D. APPLICATION AREAS AND LIMITATIONS

We formulated the polarity-dependent quadratic term of the flux-current function in the most general form mathematically possible, therefore, the proposed flux-linkage (10) and voltage equations (11) are applicable to any three-phase star-connected PMSM. The parameter identification method presented in Section IV is also applicable to any three-phase star-connected PMSM, however, it requires access to the star point of the motor and has additional hardware requirements depending on the desired accuracy. The spatial harmonic content of the elements of the abc Hessian may be dependent on the geometry and dimensions of the PMSM type. In addition, the constants appearing in the idealized Hessian (71) and in (55)–(66) also might be machine-type specific.

The presented initial position detection algorithm is applicable if the current response is fast enough to avoid rotor movement. The presented pulse-length selection method requires the knowledge of the polarity-dependent saliency coefficient Γ_0 and the standard deviation of the current measurement σ_{CM}, besides the standard model parameters. The implemented method utilizes in-line (series with the motor, see Fig. 6) measurement of all three phase-currents. Using only two in-line current sensors is possible with minimal changes in the algorithm based on Kirchhoff's first law. Using another current measurement topology, such as low-side, high-side, or DC-link current measurement, is also possible, however, it would require adapting the calculation formulae.

The algorithm is designed for zero-speed no-load condition and it is not targeting free-running. The signal injection is performed without modulation and cannot be superimposed on fundamental excitation. The algorithm determines the initial rotor position in electrical angles, not mechanical angles; for multiple pole-pair machines that means an ambiguity in the mechanical rotor position depending on the number of pole-pairs.

X. CONCLUSION

We proposed an extended PMSM model that captures the polarity-dependent saliency using a quadratic flux linkage-current function as well as successfully predicts the transient and rotor position-dependent behavior of our test motors. We managed to integrate the quadratic term of the flux model into the traditional machine modeling framework by identifying the Park and inverse Park transforms of the quadratic terms and Hessian matrices. We introduced a new machine parameter, Γ_0, to characterize the polarity-dependent saliency and presented a measurement process to determine its value. We validated the extended machine model using extensive measurement and experimental data.

A sensorless initial position detection method was developed that uses only a finite number of voltage pulses and current response measurements, moreover, does not require a sinusoidal or other high-frequency signal injection-based saturation-tracking method to determine the $+d/-d$ axis first. The method requires six voltage injection steps and current sampling occurs only once during each injection step, however, all three phase currents have to be sampled in a synchronized way.

There are many drives that have two or even just one current sensor and the neutral points of most PMSMs are not accessible. The adaptation of our method to them and the determination their Γ_0 parameter require further research. Similarly to the inductance and resistance parameters, Γ_0 is presumably frequency-dependent. The extended model may be simplified for machines that have small phase resistances by neglecting the resistive voltage drop.

The signal processing of the presented method is computationally inexpensive and can be further simplified if correcting for the winding differences is unnecessary. Our extended model may be helpful in the development of state observers that continuously monitor the magnet polarity as well as in machine design and diagnostic algorithms.

REFERENCES

[1] H. W. De Kock, M. J. Kamper, and R. M. Kennel, "Anisotropy comparison of reluctance and PM synchronous machines for position sensorless control using HF carrier injection," *IEEE T. Power Electr.*, vol. 24, no. 8, pp. 1905–1913, 2009. DOI: 10.1109/TPEL.2009.2017537.

[2] O. Lehmann, J. Schuster, and J. Roth-Stielow, "Sensorless control techniques as redundancy for the control of permanent magnet synchronous machines in electric vehicles," in *2014 IEEE Veh. Power and Propulsion Conf. (VPPC)*, 2014, pp. 1–6. DOI: 10.1109/VPPC.2014.7007127.

[3] L. Jarzebowicz, K. Karwowski, and W. J. Kulesza, "Sensorless algorithm for sustaining controllability of IPMSM drive in electric vehicle after resolver fault," *Control Eng. Pract.*, vol. 58, pp. 117–126, 2017. DOI: 10.1016/j.conengprac.2016.10.004.

[4] S. J. Rind, M. Jamil, and A. Amjad, "Electric motors and speed sensorless control for electric and hybrid electric vehicles: A review," in *2018 53rd Int. Universities Power Eng. Conf. (UPEC)*, 2018, pp. 1–6. DOI: 10.1109/UPEC.2018.8541871.

[5] Y.-S. Jeong, R. Lorenz, T. Jahns, and S.-K. Sul, "Initial rotor position estimation of an interior PM synchronous machine using carrier-frequency injection methods," *IEEE T. Ind. Appl.*, vol. 41, no. 1, pp. 38–45, 2005. DOI: 10.1109/TIA.2004.840978.

[6] R. Wu and G. R. Slemon, "A permanent magnet motor drive without a shaft sensor," *IEEE T. Ind. Appl.*, vol. 27, no. 5, pp. 1005–1011, 1991. DOI: 10.1109/28.90359.

[7] R. Bojoi, M. Pastorelli, J. Bottomley, P. Giangrande, and C. Gerada, "Sensorless control of PM motor drives – A technology status review," in *2013 IEEE Workshop on Electrical Machines Design, Control and Diagnosis (WEMDCD)*, 2013, pp. 168–182. DOI: 10.1109/WEMDCD.2013.6525177.

[8] J. Wei, H. Xu, B. Zhou, Z. Zhang, and C. Gerada, "An integrated method for three-phase AC excitation and high-frequency voltage signal injection for sensorless starting of aircraft starter/generator," *IEEE T. Ind. Electron.*, vol. 66, no. 7, pp. 5611–5622, 2019. DOI: 10.1109/TIE.2018.2871795.

[9] Y. Hua and H. Zhu, "Sensorless control of bearingless PMSM based on LS-SVM inverse system," *Electronics*, vol. 10, no. 3, 2021. DOI: 10.3390/electronics10030265.

[10] Y. Zhao, H. Yu, and S. Wang, "An improved super-twisting high-order sliding mode observer for sensorless control of permanent magnet synchronous motor," *Energies*, vol. 14, no. 19, 2021. DOI: 10.3390/en14196047.

[11] F. Briz and M. W. Degner, "Rotor position estimation – A review of high-frequency methods," *IEEE Ind. Electron. M.*, vol. 5, no. 2, pp. 24–36, 2011. DOI: 10.1109/MIE.2011.941118.

[12] J. Holtz, "Initial rotor polarity detection and sensorless control of PM synchronous machines," in *Conf. Rec. 2006 IEEE Ind. Appl. Conf. 41st IAS Annu. Meet.*, vol. 4, 2006, pp. 2040–2047. DOI: 10.1109/IAS.2006.256816.

[13] L. N. Tan, T. P. Cong, and D. P. Cong, "Neural network observers and sensorless robust optimal control for partially unknown PMSM with disturbances and saturating voltages," *IEEE T. Power Electr.*, vol. 36, no. 10, pp. 12 045–12 056, 2021. DOI: 10.1109/TPEL.2021.3071465.

[14] Y. Liu, J. Fang, K. Tan, B. Huang, and W. He, "Sliding mode observer with adaptive parameter estimation for sensorless control of IPMSM," *Energies*, vol. 13, no. 22, 2020. DOI: 10.3390/en13225991.

[15] M. Marchesoni, M. Passalacqua, L. Vaccaro, M. Calvini, and M. Venturini, "Performance improvement in a sensorless surface-mounted PMSM drive based on rotor flux observer," *Control Eng. Pract.*, vol. 96, pp. 104 276–104 286, 2020. DOI: 10.1016/j.conengprac.2019.104276.

[16] J. Dilys, V. Stankevič, and K. Łuksza, "Implementation of extended kalman filter with optimized execution time for sensorless control of a PMSM using arm cortex-m3 microcontroller," *Energies*, vol. 14, no. 12, 2021. DOI: 10.3390/en14123491.

[17] P. Vas, *Sensorless Vector and Direct Torque Control*, ser. Monographs in Electrical and Electronic Engineering. Oxford University Press, USA, 1998. ISBN: 9780198564652.

[18] G. Wang, M. Valla, and J. Solsona, "Position sensorless permanent magnet synchronous machine drives–A review," *IEEE T. Ind. Electron.*, vol. 67, no. 7, pp. 5830–5842, 2020. DOI: 10.1109/TIE.2019.2955409.

[19] R. Spießberger, A. Brunner, and M. Schrödl, "Saliency-based position sensorless control of a heavily cross-saturated PMSM," in *IECON 2021 – 47th Annu. Conf. IEEE Ind. Electron. Soc.*, 2021, pp. 1–7. DOI: 10.1109/IECON48115.2021.9589210.

[20] V. Repecho, J. B. Waqar, D. Biel, and A. Dòria-Cerezo, "Zero speed sensorless scheme for permanent magnet synchronous machine under decoupled sliding-mode control," *IEEE T. Ind. Electron.*, vol. 69, no. 2, pp. 1288–1297, 2022. DOI: 10.1109/TIE.2021.3062260.

[21] D. Basic, F. Malrait, and P. Rouchon, "Current controller for low-frequency signal injection and rotor flux position tracking at low speeds," *IEEE T. Ind. Electron.*, vol. 58, no. 9, pp. 4010–4022, 2011. DOI: 10.1109/TIE.2010.2100336.

[22] T. He and J. Chu, "Adaptive observer enhanced with low-frequency signal injection for sensorless control of PMSM," in *2019 22nd Int. Conf. Electrical Machines and Systems (ICEMS)*, 2019, pp. 1–5. DOI: 10.1109/ICEMS.2019.8921508.

[23] N. Bianchi, S. Bolognani, J.-H. Jang, and S.-K. Sul, "Comparison of PM motor structures and sensorless control techniques for zero-speed rotor position detection," *IEEE T. Power Electr.*, vol. 22, no. 6, pp. 2466–2475, 2007. DOI: 10.1109/TPEL.2007.904238.

[24] D. Xu, B. Wang, G. Zhang, G. Wang, and Y. Yu, "A review of sensorless control methods for AC motor drives," *CES Trans. Electr. Mach. Syst.*, vol. 2, no. 1, pp. 104–115, 2018. DOI: 10.23919/TEMS.2018.8326456.

[25] L. Guo, Z. Yang, and F. Lin, "A novel strategy for sensorless control of ipmsm with error compensation based on rotating high frequency carrier signal injection," *Energies*, vol. 13, no. 8, 2020. DOI: 10.3390/en13081919.

[26] M. Tursini, R. Petrella, and F. Parasiliti, "Initial rotor position estimation method for PM motors," *IEEE T. Ind. Appl.*, vol. 39, no. 6, pp. 1630–1640, 2003. DOI: 10.1109/TIA.2003.818977.

[27] M. Linke, R. Kennel, and J. Holtz, "Sensorless position control of permanent magnet synchronous machines without limitation at zero speed," in *IEEE 2002 28th Annu. Conf. Ind. Electron. Soc.*, vol. 1, 2002, pp. 674–679. DOI: 10.1109/IECON.2002.1187588.

[28] C. Zhao, M. Tanaskovic, F. Percacci, S. Mariéthoz, and P. Gnos, "Sensorless position estimation for slotless surface mounted permanent magnet synchronous motors in full speed range," *IEEE T. Power Electr.*, vol. 34, no. 12, pp. 11 566–11 579, 2019. DOI: 10.1109/TPEL.2019.2908408.

[29] Z. Wang, B. Yao, L. Guo, X. Jin, X. Li, and H. Wang, "Initial rotor position detection for permanent magnet synchronous motor based on high-frequency voltage injection without filter," *World Electr. Veh. J.*, vol. 11, no. 4, 2020. DOI: 10.3390/wevj11040071.

[30] D. Raca, M. C. Harke, and R. D. Lorenz, "Robust magnet polarity estimation for initialization of PM synchronous machines with near-zero saliency," *IEEE T. Ind. Appl.*, vol. 44, no. 4, pp. 1199–1209, 2008. DOI: 10.1109/TIA.2008.926195.

[31] M. Degner and R. Lorenz, "Using multiple saliencies for the estimation of flux, position, and velocity in AC machines," *IEEE T. Ind. Appl.*, vol. 34, no. 5, pp. 1097–1104, 1998. DOI: 10.1109/28.720450.

[32] I. Szalay, G. Kohlrusz, and D. Fodor, "Modeling of slotless surface-mounted PM synchronous motor for sensorless applications," in *2014 IEEE Int. Electric Veh. Conf.*, 2014, pp. 1–5. DOI: 10.1109/IEVC.2014.7056198.

[33] S. Murakami, T. Shiota, M. Ohto, K. Ide, and M. Hisatsune, "Encoderless servo drive with adequately designed IPMSM for pulse-voltage-injection-based position detection," *IEEE T. Ind. Appl.*, vol. 48, no. 6, pp. 1922–1930, 2012. DOI: 10.1109/TIA.2012.2226132.

[34] H. Kim, K.-K. Huh, R. Lorenz, and T. Jahns, "A novel method for initial rotor position estimation for IPM synchronous machine drives," *IEEE T. Ind. Appl.*, vol. 40, no. 5, pp. 1369–1378, 2004. DOI: 10.1109/TIA.2004.834091.

[35] S. Nakashima, Y. Inagaki, and I. Miki, "Sensorless initial rotor position estimation of surface PM synchronous motor," *IEEE T. Ind. Appl.*, vol. 36, no. 6, pp. 1598–1603, 2000. DOI: 10.1109/28.887211.

[36] Z. Wang, Z. Cao, and Z. He, "Improved fast method of initial rotor position estimation for interior permanent magnet synchronous motor by symmetric pulse voltage injection," *IEEE Access*, vol. 8, pp. 59 998–60 007, 2020. DOI: 10.1109/ACCESS.2020.2983106.

[37] P. Schmidt, M. Gasperi, G. Ray, and A. Wijenayake, "Initial rotor angle detection of a nonsalient pole PM synchronous machine," in *IAS '97. Conf. Rec. 1997 IEEE Ind. Appl. Conf. 32nd IAS Annu. Meet.*, vol. 1, 1997, pp. 459–463. DOI: 10.1109/IAS.1997.643063.

[38] W.-J. Lee and S.-K. Sul, "A new starting method of BLDC motors without position sensor," *IEEE T. Ind. Appl.*, vol. 42, no. 6, pp. 1532–1538, 2006. DOI: 10.1109/TIA.2006.882668.

[39] H. Hu, G. Xu, and B. Hu, "A new start method for sensorless brushless DC motor based on pulse injection," in *2009 Asia-Pacific Power and Energy Eng. Conf.*, 2009, pp. 1–5. DOI: 10.1109/APPEEC.2009.4918079.

[40] G. Bi, G. Wang, G. Zhang, N. Zhao, and D. Xu, "Low-noise initial position detection method for sensorless permanent magnet synchronous motor drives," *IEEE T. Power Electr.*, vol. 35, no. 12, pp. 13 333–13 344, 2020. DOI: 10.1109/TPEL.2020.2995961.

[41] S. Zossak, M. Stulraiter, P. Makys, and M. Sumega, "Initial position detection of PMSM," in *2018 IEEE 9th Int. Symp. Sensorless Control for Electrical Drives (SLED)*, 2018, pp. 12–17. DOI: 10.1109/SLED.2018.8486043.

[42] Y. Wang, N. Gao, J. Zhu, *et al.*, "Initial rotor position and magnetic polarity identification of PMS machine based on nonlinear machine model and finite element analysis," *IEEE T. Magn.*, vol. 46, no. 6, pp. 2016–2019, 2010. DOI: 10.1109/TMAG.2010.2042690.

[43] P. Kumar, O. Bottesi, S. Calligaro, L. Alberti, and R. Petrella, "Self-adaptive high-frequency injection based sensorless control for interior permanent magnet synchronous motor drives," *Energies*, vol. 12, no. 19, 2019. DOI: 10.3390/en12193645.

[44] M. Seilmeier and B. Piepenbreier, "Modeling of PMSM with multiple saliencies using a stator-oriented magnetic circuit approach," in *2011 IEEE Int. Electric Machines Drives Conf.*, 2011, pp. 131–136. DOI: 10.1109/IEMDC.2011.5994796.

[45] O. Benjak and D. Gerling, "Review of position estimation methods for PMSM drives without a position sensor, part III: Methods based on saliency and signal injection," in *2010 Int. Conf. Electrical Machines and Systems*, 2010, pp. 873–878.

[46] W. Sun, J.-X. Shen, M.-J. Jin, and H. Hao, "A robust magnetic polarity self-sensing method for start up of PM synchronous machine in fanlike system," *IEEE T. Ind. Appl.*, vol. 53, no. 3, pp. 2169–2177, 2017. DOI: 10.1109/TIA.2017.2672525.

[47] D. F. Laborda, D. Díaz Reigosa, D. Fernández, K. Sasaki, T. Kato, and F. Briz, "Enhanced torque estimation in variable leakage flux pmsm combining high and low frequency signal injection," in *2020 IEEE Energy Conversion Congr. and Expo. (ECCE)*, 2020, pp. 1764–1771. DOI: 10.1109/ECCE44975.2020.9235869.

[48] T. Wu, D. Luo, S. Huang, *et al.*, "A fast estimation of initial rotor position for low-speed free-running IPMSM," *IEEE T. Power Electr.*, vol. 35, no. 7, pp. 7664–7673, 2020. DOI: 10.1109/TPEL.2019.2958101.

[49] A. D. Polyanin and V. F. Zaitsev, *Handbook of Ordinary Differential Equations: Exact Solutions, Methods, and Problems*, 1st Ed, 2018. ISBN: 9781315117638. DOI: 10.1201/9781315117638.

ISTVÁN SZALAY earned both his B.Sc. and M.Sc. degree in mechatronics from the University of Pannonia, Veszprém, Hungary in 2011 and 2013, respectively.

Currently he is an Assistant Lecturer at the Research Institute of Automotive Mechatronics and Automation in the Faculty of Engineering at the University of Pannonia, Veszprém, Hungary. His current research interests include permanent magnet synchronous motor drives, position sensorless control methods, and electrification of road vehicles.

DÉNES FODOR (M'92–SM'20) holds a D.Sc. degree (2001-Magna Cum Laude) in electrical engineering from the Technical University of Cluj-Napoca, Romania, and an M. Sc. degree (1989) from the same university.

Currently, he is the Head of the Research Institute of Automotive Mechatronics and Automation in the Faculty of Engineering at the University of Pannonia, Veszprém, Hungary. He is the Head of the School of Automotive System Engineering and leads the Software Sensors Research Group at the same university. His research interests are the control of power electronics and drives, motion control, industrial and automotive communication systems, signal processing, automotive electronic systems and autonomous vehicles.

Dr. Fodor is the author of one book entitled Modern Power Electronics, eight university students' books, six book chapters and more than 170 scientific publications as well as serves as a Ph.D. supervisor.

KRISZTIÁN ENISZ earned a degree in information technology from University of Pannonia, Veszprém, Hungary, in 2010 and the Ph.D. degree in chemical engineering and material science from the same university in 2016.

Currently, he is a Research Fellow with the Research Institute of Automotive Mechatronics and Automation, University of Pannonia, Veszprém, Hungary. His research interests include test system development, hardware-in-the-loop simulations and the development of automotive electronic control units.

HUNOR MEDVE earned both his B.Sc. in electrical engineering and subsequently his M.Sc. in mechatronics engineering from the University of Pannonia, Veszprém, Hungary. After his studies, he gained substantial industrial experience abroad at market-leading companies in the field of electronics as well as in automotive, development, manufacturing, strategic procurement and sales.

Since 2019, he is a Research Fellow at the Research Institute of Automotive Mechatronics and Automation at the University of Pannonia, Veszprém, Hungary. His research interests are electrical drives, energy conversion, state estimation and diagnostics.